Supporting Information

Fast-Switching Vis–IR Electrochromic Covalent Organic Frameworks

Derya Bessinger[1], Katharina Muggli[1], Michael Beetz[1], Florian Auras[2]*, and Thomas Bein[1]*

[1]Department of Chemistry and Center for NanoScience (CeNS), University of Munich (LMU), Butenandtstraße 5-13, 81377 Munich, Germany
[2]Cavendish Laboratory, University of Cambridge, Cambridge CB3 0HE, United Kingdom
*e-mail: fa355@cam.ac.uk, bein@lmu.de

Table of contents

A	Methods	2	H	Switching speed and stability	17
B	COF syntheses	3	I	Coloration efficiency and extracted charge	19
C	COF structure analysis	5	J	Building block syntheses	21
D	IR spectroscopy	9	K	NMR spectra of the TII building blocks	26
E	UV-Vis spectroscopy	10	L	Solid-state NMR	28
F	COF films and GIWAXS analysis	11	M	References	29
G	Spectroelectrochemistry	12			

Abbreviations

BET	Brunauer-Emmett-Teller	NIR	near-infrared
CV	cyclic voltammetry	OD	optical density
dba	dibenzylideneacetone	PSD	pore size distribution
DCM	dichloromethane	PTFE	poly(tetrafluoroethylene)
DMF	*N*,*N*-dimethylformamide	QSDFT	quenched solid density functional theory
DMSO	dimethyl sulfoxide	rt	room temperature
eq.	equivalents	SPhos	dicyclohexylphosphino-2',6'-dimethoxybiphenyl
fc	ferrocene	$TBAPF_6$	tetrabutylammonium hexafluorophosphate
ICT	intramolecular charge transfer	TFA	trifluoroacetic acid
ITO	indium tin oxide	THF	tetrahydrofuran
LDA	lithium diisopropylamide	tol	tolyl
NBS	*N*-bromosuccinimide		

COF building blocks

$Py(NH_2)_4$	1,3,6,8-tetrakis(4-aminophenyl)pyrene
$N(CHO)_2$	naphthalene-2,6-dicarbaldehyde
$nTII(CHO)_2$	5,5'-bis(2-formylnaphthalen-6-yl)-*N*,*N*'-dihexyl-thienoisoindigo
$TII(CHO)_2$	5,5'-diformyl-*N*,*N*'-dihexyl-thienoisoindigo
$TT(CHO)_2$	thieno[3,2-*b*]thiophene-2,5-dicarbaldehyde
$ttTII(CHO)_2$	5,5'-bis(2-formylthienothiophen-5-yl)-*N*,*N*'-dihexyl-thienoisoindigo

A. Methods

Nuclear magnetic resonance (NMR) spectra were recorded on Bruker Avance III HD spectrometers. Proton chemical shifts are expressed in parts per million (δ scale) and are calibrated using residual undeuterated solvent peaks as an internal reference (^{1}H NMR: $CDCl_3$: 7.26, DMSO-d_6: 2.50; ^{13}C NMR: $CDCl_3$: 77.2, DMSO-d_6: 39.5). Data for ^{1}H NMR spectra are reported in the following way: chemical shift (δ ppm) (multiplicity, coupling constant, integration). Multiplicities are reported as follows: s = singlet, d = doublet, t = triplet, q = quartet, m = multiplet, or combinations thereof.

Solid-state ^{13}C cross-polarization magic angle spinning (CP-MAS) NMR spectra were recorded with a Bruker Avance III-500 spectrometer using 4 mm diameter ZrO_2 rotors at a spinning frequency of 12 kHz.

Powder X-ray diffraction (PXRD) patterns were measured on a Bruker D8 Advance diffractometer equipped with a Cu K_α source (0.1 mm divergence slit, knife edge air scatter screen) and a LynxEye detector. K_β radiation was attenuated with a 0.0125 mm Ni filter.

2D grazing-incidence wide angle X-ray scattering (GIWAXS) data were recorded with an Anton Paar SAXSpoint 2.0 system equipped with a Primux 100 micro Cu K_α source and a Dectris EIGER R 1M detector. The COF films were positioned at a sample-detector distance of 140 mm and were measured with an incidence angle of 0.2°.

The **structure models of the COFs** were constructed using the Accelrys Materials Studio software package. For each COF, the highest possible symmetry was applied considering the rotation of the bridge units vs. the pyrene cores. The structure models were optimized using the Forcite module with the Dreiding force-field. **Structure refinements** were carried out with the Reflex module using the Rietveld method. Pseudo-Voigt peak profiles were used, and peak asymmetry was corrected using the Finger-Cox-Jephcoat method. **Connolly surfaces** and accessible surfaces were generated using a N_2-sized probe (r = 0.184 nm) at a 0.025 nm grid interval.[1]

Nitrogen sorption isotherms were recorded with Quantachrome Autosorb 1 and Autosorb iQ instruments at 77 K. The samples were extracted with supercritical CO_2 for 1 h, followed by degassing at 100 °C under high vacuum for 1 h prior to the measurements. BET areas were calculated based on the pressure range $0.05 \leq p/p_0 \leq 0.2$. Pore size distributions were calculated using the QSDFT equilibrium model (desorption) with a carbon kernel for cylindrical pores.

Scanning electron microscopy (SEM) images were obtained with an FEI Helios NanoLab G3 UC microscope equipped with a Schottky field-emission electron source operated at 1 – 30 kV.

Transmission electron microscopy (TEM) images were obtained with an FEI Titan Themis microscope equipped with a field emission gun operated at 300 kV.

Infrared (IR) spectra were recorded on a Thermo Scientific Nicolet iN10 FT-IR spectrometer equipped with a MicroTip attenuated total reflection (ATR) unit and an MCT-detector. The spectra were analyzed with the OMNIC software package.

UV-Vis-NIR spectra were recorded on a Perkin-Elmer Lambda 1050 spectrometer equipped with a 150 mm InGaAs integrating sphere. Absorbance spectra of the starting materials were measured with 50 µM chloroform solutions. **Diffuse reflectance spectra** were recorded with a Harrick Praying Mantis accessory kit and were referenced to barium sulfate powder as the white standard.

Electrochemical measurements were performed with a Metrohm Autolab PGSTAT potentiostat/galvanostat. **Cyclic voltammetry (CV)** scans were recorded with the respective COF film on ITO or Au/glass as the working electrode, a Pt wire counter electrode and a Ag/AgCl reference electrode. 0.1 M tetrabutylammonium hexafluorophosphate ($TBAPF_6$) in MeCN was chosen as the electrolyte. 0.1 mM ferrocene solution was used as a standard in control experiments with a blank ITO working electrode. All potentials are referenced to the fc/fc^+ redox pair ($V_{fc/fc+}$ = +0.50 V vs. Ag/Ag^+).

For the **spectroelectrochemical measurements**, the COF films were placed inside a fused silica cuvette (20 mm path length) equipped with a Pt wire counter electrode, Ag/AgCl (3 M NaCl) reference electrode and 0.1 M $TBAPF_6$/MeCN electrolyte. The potential was increased/decreased in 200 mV intervals using a 20 mV s^{-1} ramp and then held constant for the duration of the UV-Vis scan (ca. 5 min per spectrum). For the **stability and response time measurements**, the applied potential was switched between -200 mV and +1V vs. Ag/AgCl and held constant for 2 s between each step. In order to reduce the instrument response time, absorption changes were tracked with the Lambda 1050 photomultiplier tube (Vis) and InGaAs (NIR) detectors set to fixed gain mode.

B. COF syntheses

Reagents and solvents were obtained in high-purity grades from commercial suppliers and were, unless shipped under argon, degassed and saturated with argon prior to use. The COF building blocks were synthesized as detailed in Section C. Thieno[3,2-*b*]thiophene-2,5-dicarbaldehyde ($TT(CHO)_2$) was obtained from Merck and purified by recrystallization from hot DMF. 1,3,6,8-tetrakis(4-aminophenyl)pyrene ($Py(NH_2)_4(dioxane)_{1.5}$) and naphthalene-2,6-dicarbaldehyde ($N(CHO)_2$) were synthesized according to published procedures.[2-3] Please refer to page S1 for a list of abbreviations for the COF building blocks and solvents.

COF bulk powder syntheses were performed under argon atmosphere in PTFE-sealed glass reaction tubes (6 mL volume).

COF thin films were synthesized in 100 mL autoclaves equipped with a 28 mm diameter glass liner. ITO-coated glass substrates were cleaned in detergent solution (Hellmanex III, 0.5% *v*/*v*), water, acetone, and isopropanol, and activated with an O_2-plasma for 5 min directly before use. Semi-transparent gold substrates were prepared by thermal evaporation of a 3 nm Ti layer, followed by a 10 nm Au layer. The gold substrates were activated with an O_2-plasma for 5 min directly before use. For the COF thin film syntheses, substrates were placed horizontally in PTFE sample holders with the activated surface face-down.

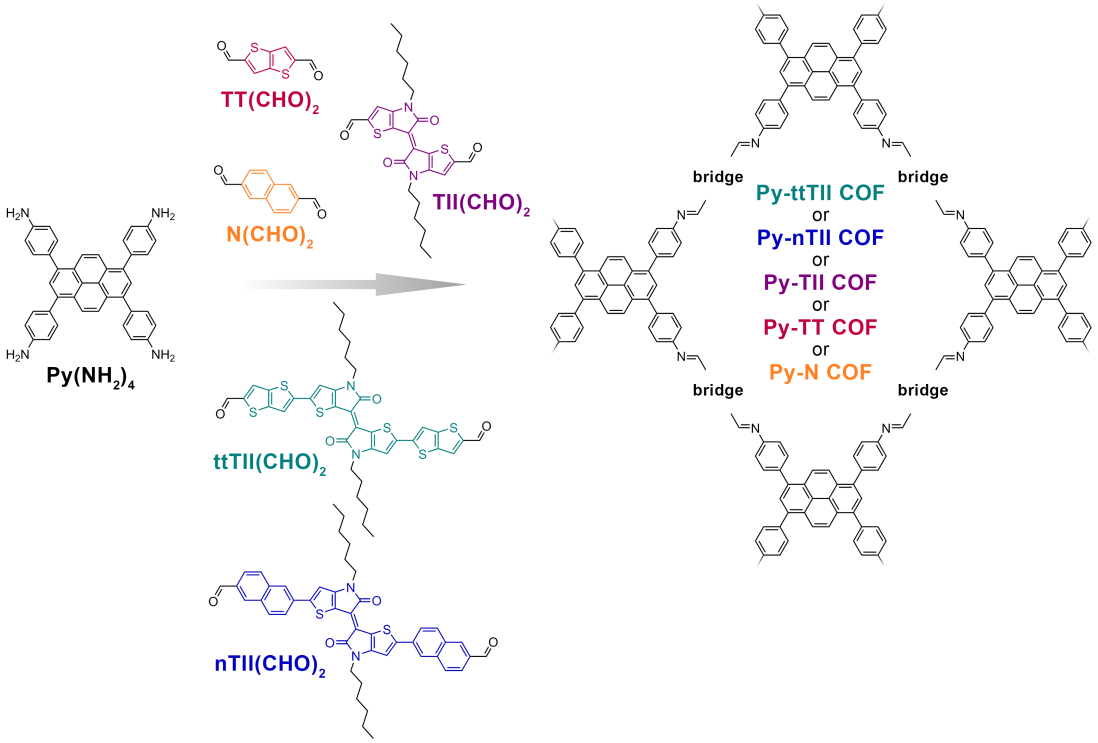

Figure S1. Construction of the new thienoisoindigo-based COFs and smaller-pore reference materials. The co-condensation of the tetradentate $Py(NH_2)_4$ with the linear dialdehyde building blocks yields the Py-ttTII, Py-nTII, Py-TII, Py-TT and Py-N COFs, respectively.

Py-ttTII COF. $Py(NH_2)_4(dioxane)_{1.5}$ (14.0 mg, 20 µmol, 1.0 eq.) and $ttTII(CHO)_2$ (31.0 mg, 40 µmol, 2.0 eq.) were filled into a 6 mL reaction tube, followed by the addition of mesitylene (667 µL), benzyl alcohol (333 µL), and 6 M acetic acid (100 µL). The tube was sealed and heated at 120 °C for 6 d. After cooling to room temperature, the precipitate was collected by filtration, washed with MeCN and dried in air. Extraction with supercritical CO_2 for 1 h yielded the COF as a dark green powder.

Elemental analysis (calculated, found for $C_{232}H_{180}N_{16}O_8S_{24}$): C (68.14, 67.48), H (4.44, 4.53), N (5.48, 5.23), S (18.81, 18.37).

Py-ttTII COF films. An autoclave was charged with $Py(NH_2)_4(dioxane)_{1.5}$ (3.5 mg, 5 µmol, 1.0 eq.), $ttTII(CHO)_2$ (7.8 mg, 10 µmol, 2.0 eq.), mesitylene (1333 µL) and benzyl alcohol (667 µL). An ITO/glass substrate was inserted, followed by the addition of 6 M acetic acid (200 µL). The autoclave was sealed and heated at 120 °C for 3 d. After cooling to room temperature, the COF film was rinsed with dry MeCN and dried with a stream of nitrogen.

The COF film thickness is 430 ± 30 nm (determined by cross-sectional SEM, sample-to-sample variation by UV-Vis).

Py-nTII COF. $Py(NH_2)_4(dioxane)_{1.5}$ (14.0 mg, 20 µmol, 1.0 eq.) and $nTII(CHO)_2$ (30.0 mg, 40 µmol, 2.0 eq.) were filled into a 6 mL reaction tube, followed by the addition of mesitylene (333 µL), 1,4-dioxane (667 µL), and 6 M acetic acid (100 µL). The tube was sealed and heated at 120 °C for 6 d. After cooling to room temperature, the precipitate was collected by filtration, washed with MeCN and dried in air. Extraction with supercritical CO_2 for 1 h yielded the COF as a dark green powder.

Elemental analysis (calculated, found for $C_{264}H_{212}N_{16}O_8S_8$): C (79.41, 77.13), H (5.35, 5.36), N (5.61, 5.35), S (6.42, 6.47).

Py-nTII COF films. An autoclave was charged with $Py(NH_2)_4(dioxane)_{1.5}$ (3.5 mg, 5 µmol, 1.0 eq.), $nTII(CHO)_2$ (7.5 mg, 10 µmol, 2.0 eq.), mesitylene (1333 µL) and benzyl alcohol (667 µL). A gold/glass substrate was inserted, followed by the addition of 6 M acetic acid (200 µL). The autoclave was sealed and heated at 120 °C for 3 d. After cooling to room temperature, the COF film was immersed in dry MeCN for 2 min and dried with a stream of nitrogen.

The COF film thickness is 280 ± 30 nm (determined by cross-sectional SEM; sample-to-sample variation by UV-Vis).

Py-TII COF. $Py(NH_2)_4(dioxane)_{1.5}$ (14.0 mg, 20 µmol, 1.0 eq.) and $TII(CHO)_2$ (20.0 mg, 40 µmol, 2.0 eq.) were filled into a 6 mL reaction tube, followed by the addition of mesitylene (667 µL), benzyl alcohol (333 µL), and 6 M acetic acid (100 µL). The tube was sealed and heated at 120 °C for 6 d. After cooling to room temperature, the precipitate was collected by filtration, washed with MeCN and extracted with supercritical CO_2 for 1 h to yield the COF as a dark teal powder.

Elemental analysis (calculated, found for $C_{184}H_{164}N_{16}O_8S_8$): C (74.06, 72.28), H (5.54, 5.49), N (7.51, 7.02), S (8.60, 8.35).

Py-TII COF films. An autoclave was charged with $Py(NH_2)_4(dioxane)_{1.5}$ (3.5 mg, 5 µmol, 1.0 eq.), $TII(CHO)_2$ (5.0 mg, 10 µmol, 2.0 eq.), mesitylene (1333 µL) and benzyl alcohol (667 µL). An ITO/glass substrate was inserted, followed by the addition of 6 M acetic acid (200 µL). The autoclave was sealed and heated at 120 °C for 3 d. After cooling to room temperature, the COF film was immersed in dry MeCN for 2 min and dried with a stream of nitrogen.

Py-TT COF. This COF was prepared according to literature procedures.[4]

Py-TT COF films. COF thin films were prepared according to literature procedures.[4]

Py-N COF. $Py(NH_2)_4(dioxane)_{1.5}$ (14.0 mg, 20 µmol, 1.0 eq.) and $N(CHO)_2$ (7.4 mg, 40 µmol, 2.0 eq.) were filled into a 6 mL reaction tube, followed by the addition of mesitylene (667 µL), benzyl alcohol (333 µL), and 6 M acetic acid (100 µL). The tube was sealed and heated at 120 °C for 6 d. After cooling to room temperature, the precipitate was collected by filtration, washed with MeCN and dried in air. Extraction with supercritical CO_2 for 1 h yielded the COF as an orange-red powder.

Elemental analysis (calculated, found for $C_{128}H_{76}N_8$): C (89.07, 86.90), H (4.44, 4.29), N (6.49, 6.21)

Py-N COF films. An autoclave was charged with $Py(NH_2)_4(dioxane)_{1.5}$ (3.5 mg, 5 µmol, 1.0 eq.), $N(CHO)_2$ (1.8 mg, 10 µmol, 2.0 eq.), mesitylene (1333 µL) and benzyl alcohol (667 µL). An ITO/glass or fused silica substrate was inserted, followed by the addition of 6 M acetic acid (200 µL). The autoclave was sealed and heated at 120 °C for 3 – 4 d. After cooling to room temperature, the COF film was immersed in dry MeCN for 2 min and dried with a stream of nitrogen.

C. COF structure analysis

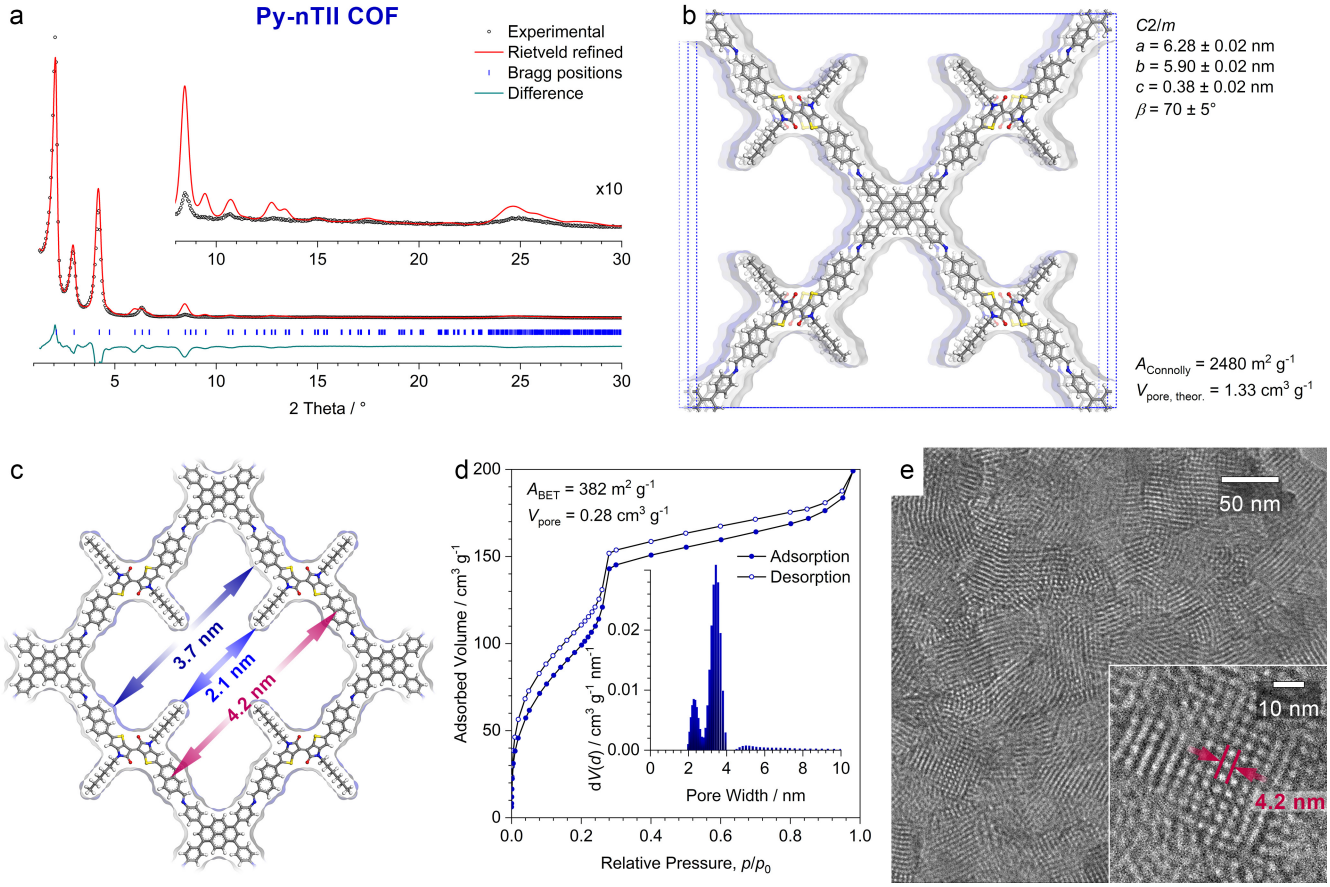

Figure S2-1. Structure analysis of the Py-nTII COF.

(**a**) PXRD pattern of the Py-nTII COF bulk material (black dots). Rietveld refinement (red line) using the monoclinic (space group *C*2/*m*) structure model shown on the right provides a good fit, with only small differences between the experimental and refined patterns (green line) arising mainly from the flexibility of the alkyl chains. R_{wp} = 13.7%, R_p = 23.5%. Bragg positions are indicated by blue ticks. Inset: Magnified view of the 2θ > 8° region.

(**b**) The Rietveld-refined structure model of the Py-nTII COF viewed perpendicular to the crystallographic *a*-*b* plane. The COF has a pseudo-square geometry with slip-stacked layers. The structure is highly porous with a Connolly surface of 2480 $m^2\ g^{-1}$ and a pore volume of 1.33 $cm^3\ g^{-1}$.

(**c**) Illustration of the pore structure of the COF viewed along the *c*-axis. The structure refinement indicates that in this COF the alkyl chains extend relatively straight into the pores, producing a shamrock-shaped pore cross-section. The wall-to-wall distances (blue arrows) are 2.1 nm and 3.7 nm including and excluding the alkyl chains, respectively. The periodicity of the COF in this orientation is 4.2 nm (red arrows).

(**d**) Nitrogen sorption isotherm recorded at 77 K. The BET area and total pore volume are reduced compared to the structure model, most likely due to oligomeric fragments that were enclosed in the pores during the synthesis. This is a common challenge for COFs based on extended, bulky building blocks with low solubility.[5] Inset: Fitting the isotherm with a QSDFT equilibrium model for cylindrical pores produces a bimodal pore size distribution (PSD) with peaks at 2.3 nm and 3.5 nm. While unexpected at first glance, this PSD is a result of the algorithm trying to express the non-cylindrical pores as a superposition of cylindrical pores with the two contributions being in good agreement with the wall-to-wall distances including and excluding the alkyl chains. Bimodal PSDs have been observed previously for alkyl-containing COFs.[6] The sorption data and PSD analysis hence confirm the shamrock-shaped pore cross-section and provide an independent validation of the XRD-derived structure model of the Py-nTII COF.

(**e**) High-resolution TEM image of a Py-nTII COF bulk powder sample showing crystallites of 50-100 nm diameter. Inset: Magnified image of a crystallite viewed along the pores (i.e., along the crystallographic *c*-axis) showing a periodicity of 4.2 nm in excellent agreement with the structure model.

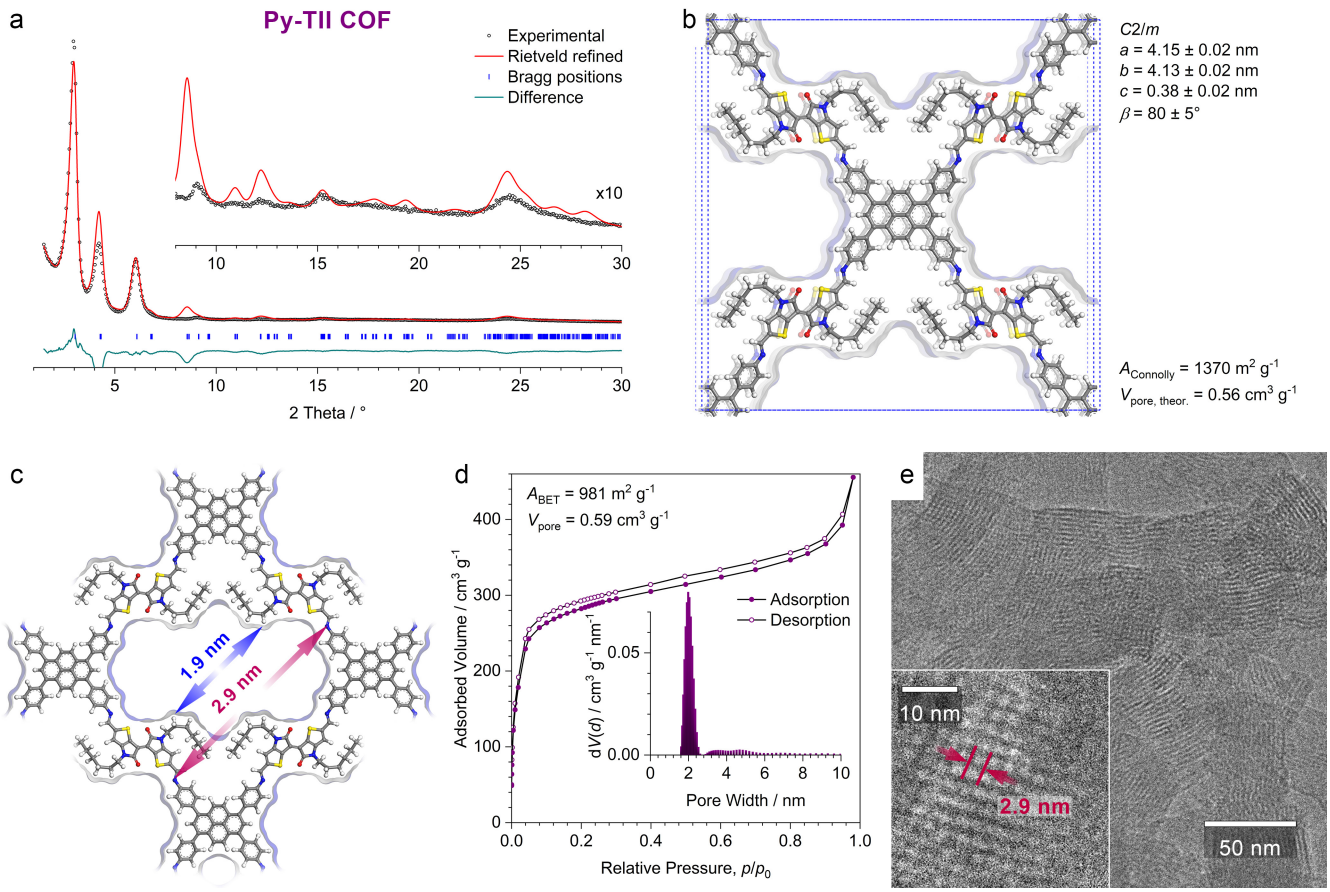

Figure S2-2. Structure analysis of the Py-TII COF.

(**a**) PXRD pattern of the COF bulk material (black dots). Rietveld refinement (red line) using the monoclinic (space group *C*2/*m*) structure model shown on the right provides a good fit, with only small differences between the experimental and refined patterns (green line). R_{wp} = 15.3%, R_p = 23.9%. Bragg positions are indicated by blue ticks. Inset: Magnified view of the 2θ > 8° region.

(**b**) The Rietveld-refined structure model of the Py-TII COF viewed perpendicular to the crystallographic *a*-*b* plane. The COF has a pseudo-square geometry with slip-stacked layers. The PXRD data quality is sufficient to refine the location of groups of atoms such as the hexyl chains. In this COF, the alkyl chains do not extend straight into the pore but collapse towards the neighboring pyrene units. This arrangement might be favorable because it avoids close contacts between the alkyl chains and the division of the pores into four small compartments. The COF is porous with a Connolly surface of 1370 $m^2 g^{-1}$ and a pore volume of 0.56 $cm^3 g^{-1}$.

(**c**) Illustration of the pore structure viewed along the *c*-axis. The collapsed alkyl chains produce a pore with 1.9 nm wall-to-wall distance (blue arrows). The periodicity of the COF in this orientation is 2.9 nm (red arrows).

(**d**) Nitrogen sorption isotherm recorded at 77 K. The BET area and pore volume are in good agreement with the porosity expected from the structure model. Inset: Fitting the isotherm with a QSDFT equilibrium model for cylindrical pores yields a narrow PSD with a maximum at 2.0 nm, in excellent agreement with the structure model. The fact that, in contrast to the larger Py-ttTII and Py-nTII COFs, the QSDFT analysis does not produce a bimodal distribution validates the XRD-derived structure model and confirms that the hexyl chains are collapsed to the pore walls in this COF.

(**e**) High-resolution TEM image of a Py-TII COF bulk powder sample showing crystallites of about 50 nm diameter. Inset: Magnified image of a crystallite viewed along the pores (i.e., along the crystallographic *c*-axis) showing a periodicity of 2.9 nm in excellent agreement with the structure model.

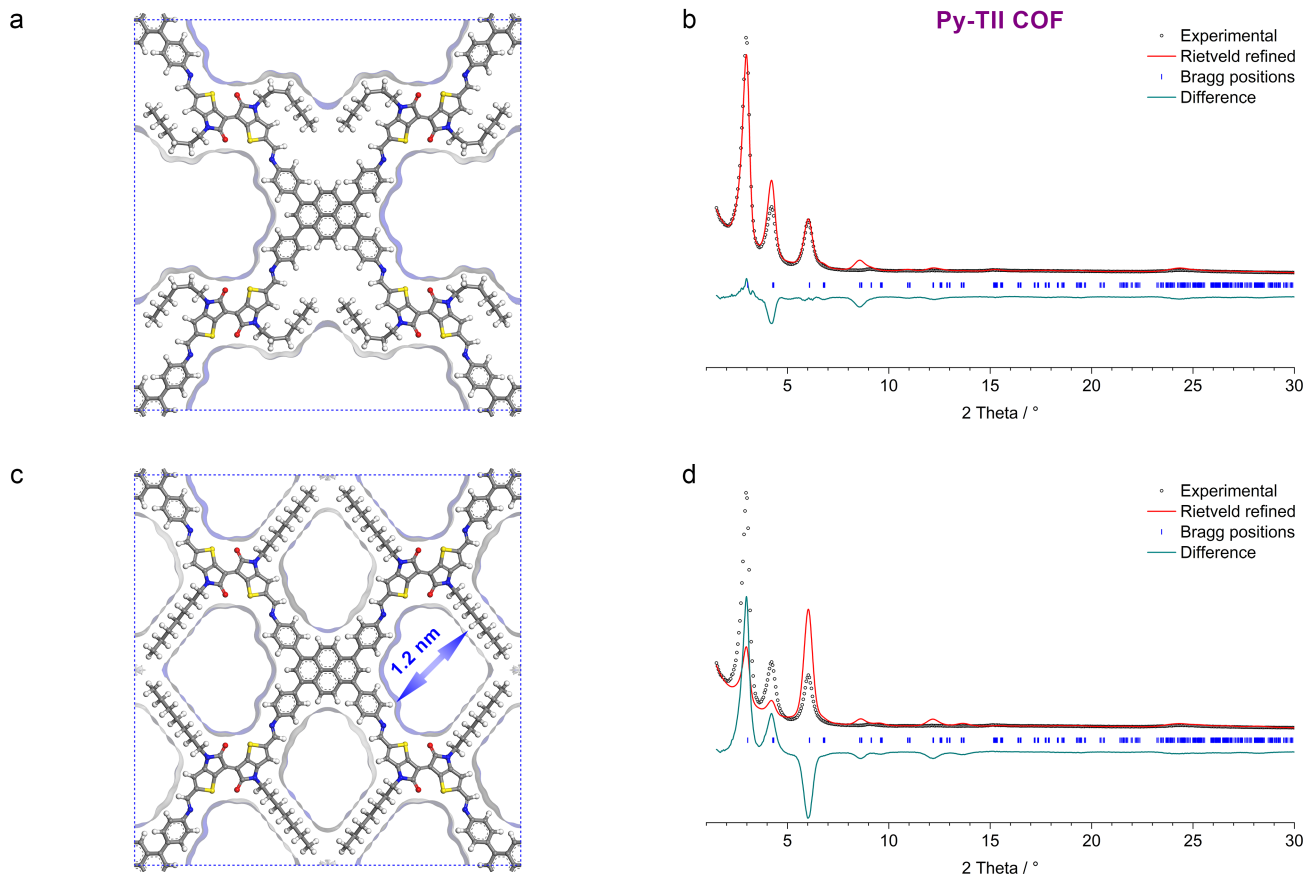

Figure S2-3. Comparison between the Py-TII COF structure models.
(**a**) Structure model of the Py-TII COF with collapsed alkyl chains. The Connolly surface calculated for an N_2-sized molecule is shown in blue. This arrangement of the alkyl chains leads to a large, slightly slit-like pore.
(**b**) This structure model provides a good fit to the experimental PXRD data and is further supported by the nitrogen sorption data (Figure S2-2d).
(**c**) Hypothetical structure model of the COF with the alkyl chains extending straight into the pore. In contrast to the larger COFs, this configuration would divide the pore of the Py-TII COF into four microporous compartments.
(**d**) Due to the very different distribution of electron density in the pores, this structure would lead to significantly different reflection intensities (red line) which do not match the experimental pattern. Moreover, straight alkyl chains can be excluded based on the nitrogen sorption, which clearly shows a pore width of around 2 nm (Figure S2-2d).

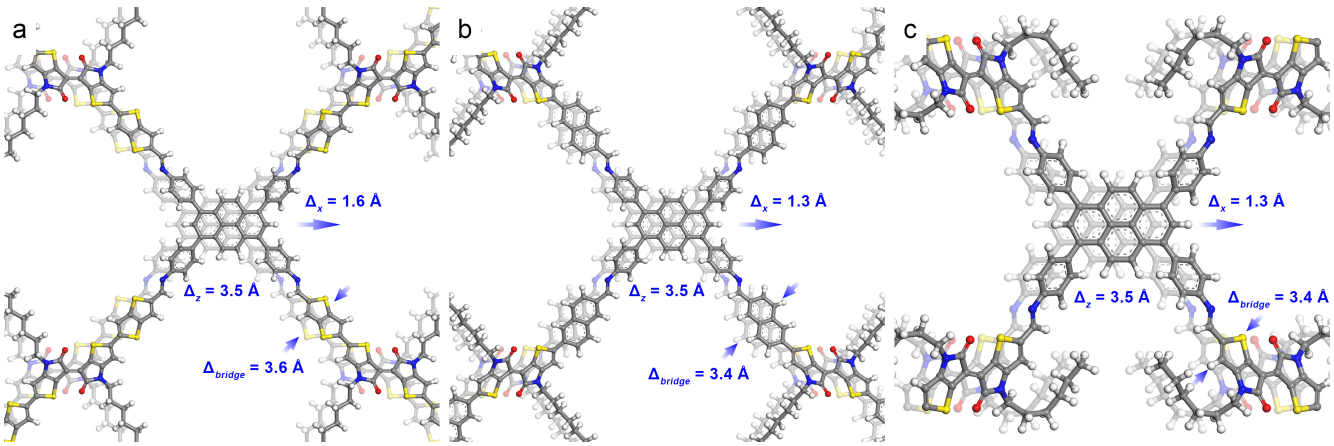

Figure S2-4. Stacking distances in the thienoisoindigo COFs. (**a**) Py-ttTII COF, (**b**) Py-nTII COF, (**c**) Py-TII COF. In all COFs, the pyrene-to-pyrene π-stacking distance (Δ_z; measured perpendicular to the pyrene planes) is 3.5 Å. The distance between the thienoisoindigo bridge units (measured perpendicular to the TII planes) ranges from 3.4 to 3.6 Å, confirming that also these moieties are closely packed in all three COFs. The lateral layer offset ranges from 1.3 Å in the Py-nTII and Py-TII COFs to 1.6 Å for the Py-ttTII COF. Given the very similar packing geometries, the electronic coupling across the COF layers is expected to be comparable in all three COFs.

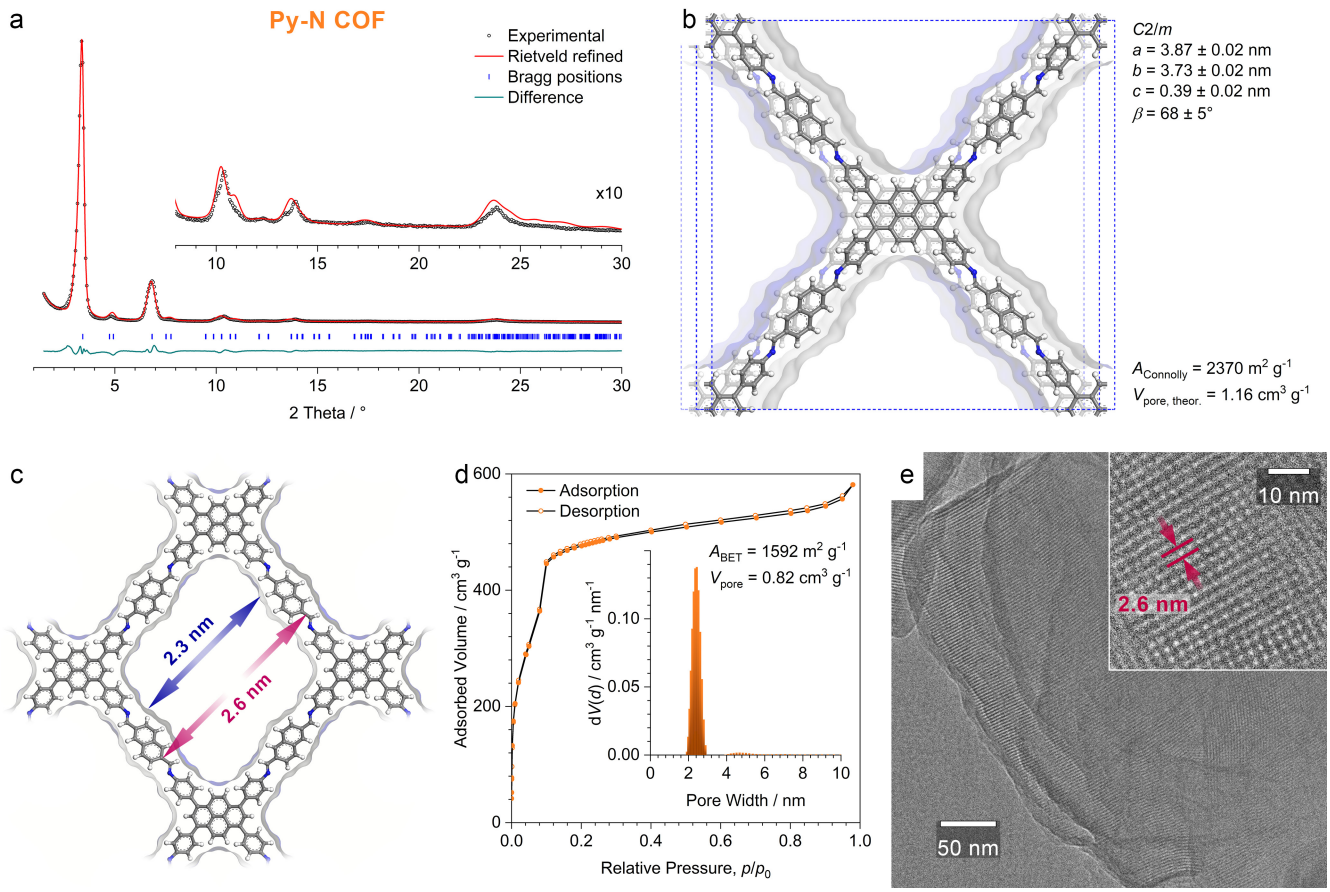

Figure S2-5. Structure analysis of the Py-N COF.

(**a**) PXRD pattern of the COF bulk material (black dots). Rietveld refinement (red line) using the monoclinic (space group *C*2/*m*) structure model shown on the right provides a very good fit, with only minimal differences between the experimental and refined patterns (green line). R_{wp} = 4.0%, R_p = 12.5%. Bragg positions are indicated by blue ticks. Inset: Magnified view of the 2θ > 8° region.

(**b**) The Rietveld-refined structure model of the Py-N COF viewed perpendicular to the crystallographic *a*-*b* plane. The COF has a pseudo-square geometry with slip-stacked layers. The COF is highly porous with a Connolly surface of 1910 $m^2 g^{-1}$ and a pore volume of 0.61 $cm^3 g^{-1}$.

(**c**) Illustration of the pore structure viewed along the *c*-axis. The pores have a pseudo-square cross-section with a wall-to-wall distance of 2.3 nm. The periodicity of the COF in this orientation is 2.6 nm (red arrows).

(**d**) Nitrogen sorption isotherm recorded at 77 K. The BET area and pore volume are in good agreement with the porosity expected from the structure model. Inset: Fitting the isotherm with a QSDFT equilibrium model for cylindrical pores yields a narrow PSD with a maximum at 2.4 nm, which is in excellent agreement with the structure model.

(**e**) High-resolution TEM image of a Py-N COF bulk powder sample showing large crystal domains of about 400 nm. Inset: Magnified image of a crystallite viewed along the pores (i.e., along the crystallographic *c*-axis) showing a periodicity of 2.6 nm in excellent agreement with the structure model.

Other COFs:

See the manuscript for the structure analysis of the Py-ttTII COF.

The structure analysis of the Py-TT COF has been published previously.[4]

D. IR spectroscopy

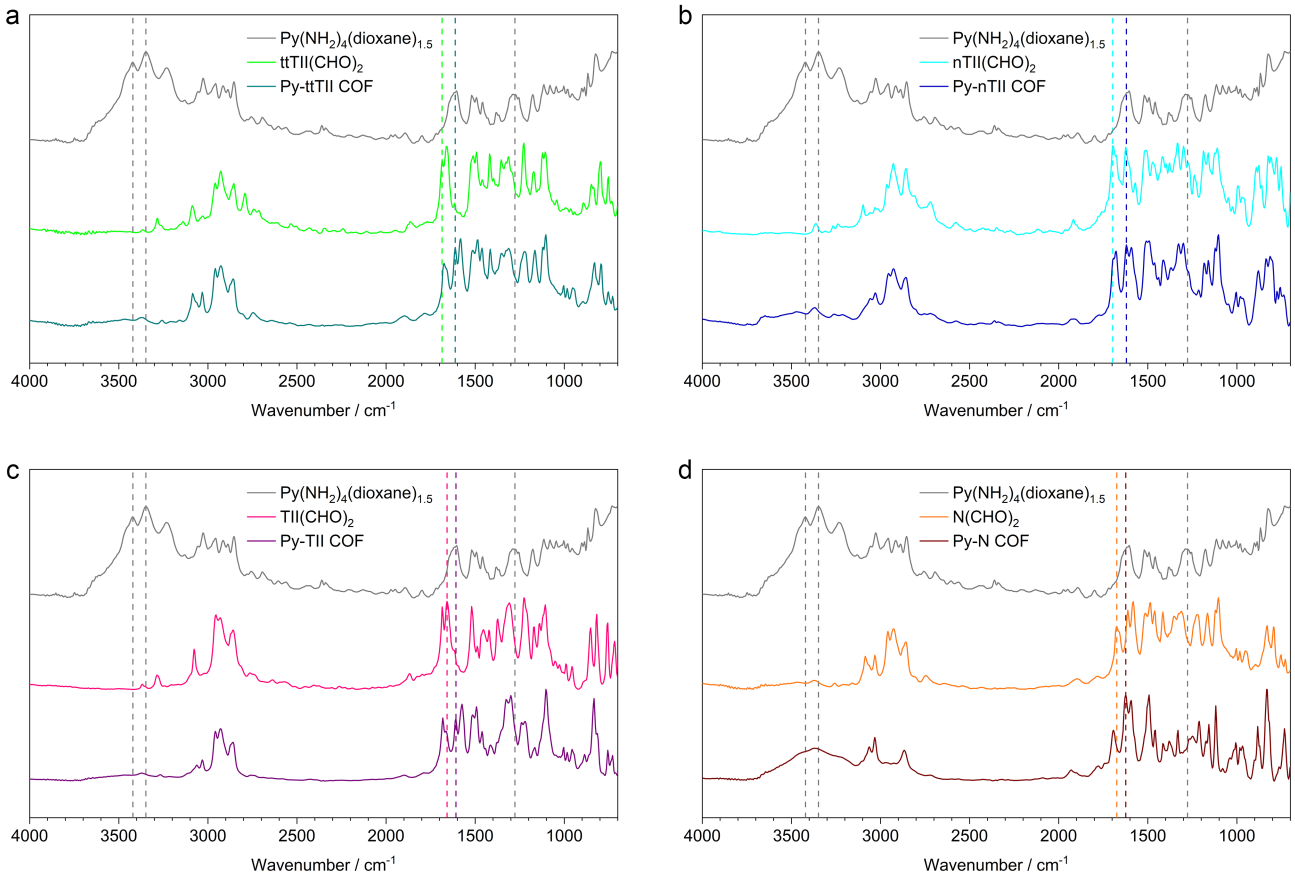

Figure S3. Comparison of IR spectra of the precursors and their COF powders. The IR spectra of the building blocks show the characteristic C-NH_2 and C=O stretching vibrations of the amine ($Py(NH_2)_4$) and aldehyde (linear precursors) functional groups, respectively. The attenuation of these absorption signals and the evolution of the C=N stretching vibrations of the imine bonds at around 1610 cm^{-1} confirm the successful COF formation.

Table S1. Assignments of selected IR signals.

	Wavenumber / cm^{-1}	Assignment
$Py(NH_2)_4(dioxane)_{1.5}$	1277 3348 3421	C–NH_2 stretching N-H stretching N-H stretching
$ttTII(CHO)_2$	1686	C=O stretching
Py-ttTII COF	1612	C=N stretching
$nTII(CHO)_2$	1697	C=O stretching
Py-nTII COF	1620	C=N stretching
$TII(CHO)_2$	1658	C=O stretching
Py-TII COF	1608	C=N stretching
$N(CHO)_2$	1674	C=O stretching
Py-N COF	1624	C=N stretching

E. UV-Vis spectroscopy

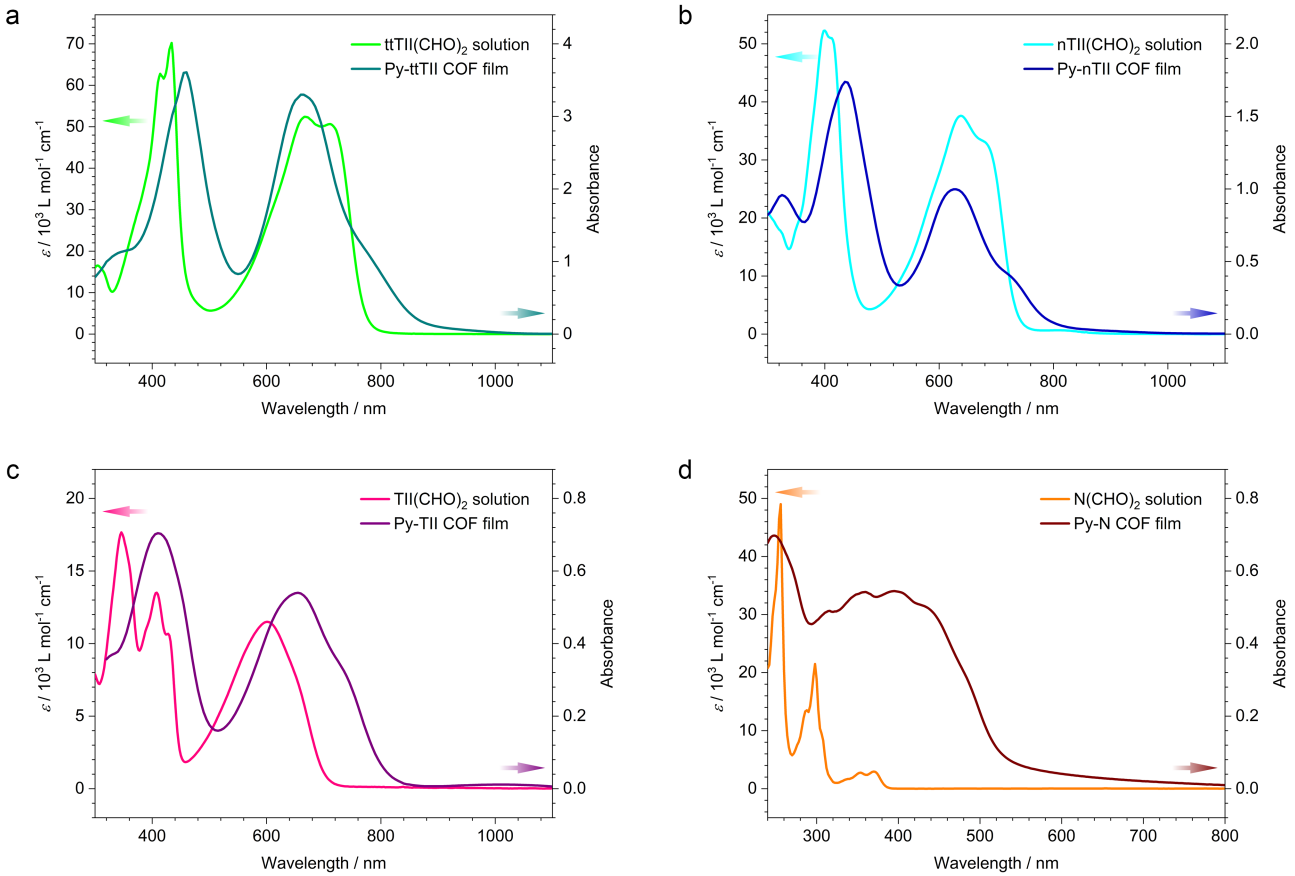

Figure S4. Comparison of the absorption spectra of the building blocks (50 µM solutions in $CHCl_3$) and the corresponding COF thin films. (**a**) Py-ttTII COF grown on ITO, (**b**) Py-nTII COF on a 10 nm Au layer, (**c**) Py-TII COF on ITO, (**d**) Py-N COF on fused silica.

The thienoisoindigo-containing building blocks have two characteristic absorption bands. The higher-energy band between 330 and 500 nm can be attributed to π–π* transitions, whereas the strong absorption at longer wavelengths starting at 500 nm and ranging into the NIR is due to intramolecular charge transfer (ICT) between electron-rich and -deficient moieties. These ICT transitions are enabled by the structure design of the TII-based building blocks with their strongly electron-accepting ketopyrrole cores and the electron-donating fused thiophenes in the TII, or the coupled thienothiophenes and naphthalenes in the ttTII and nTII building blocks, respectively.

F. COF films GIWAXS analysis

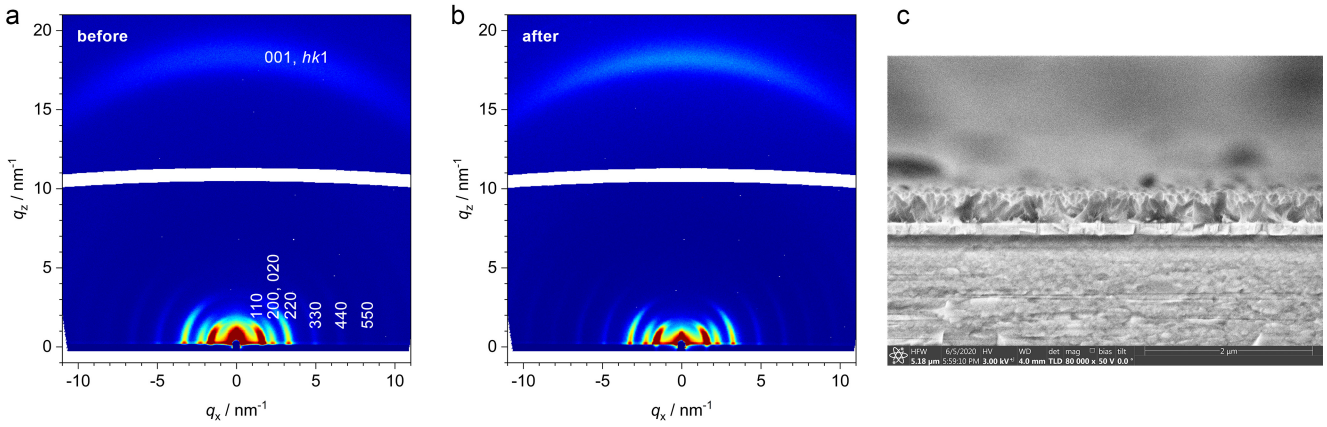

Figure S5-1. 2D GIWAXS patterns of a Py-ttTII COF film on ITO (**a**) before and (**b**) after 200 electrochemical oxidation/reduction cycles. The film is polycrystalline and highly textured with the COF *a-b* planes predominantly aligned parallel to the substrate. The crystallinity and orientation are fully retained during the electrochemical switching. (**c**) SEM cross-section of a Py-ttTII COF film. In contrast to other COFs, films of this COF are not dense, but have a pillar-like morphology.

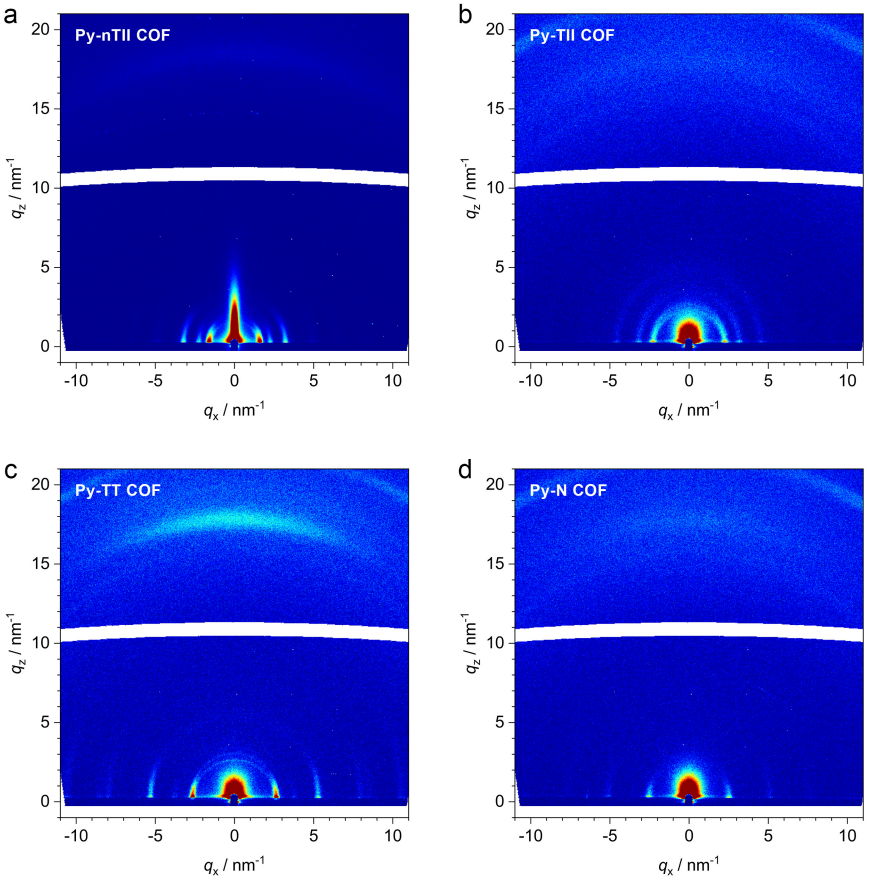

Figure S5-2. 2D GIWAXS patterns of the other COFs after ten oxidation/reduction cycles. (**a**) Py-nTII COF on a 10 nm Au/glass substrate. (**b**) Py-TII COF on ITO. (**c**) Py-TT COF on ITO. (**d**) Py-N COF on ITO. The COF films are polycrystalline and strongly textured with the *a-b* planes predominantly parallel to the substrate surface. Thus, the pores extend towards the film surface and are accessible.

G. Spectroelectrochemistry

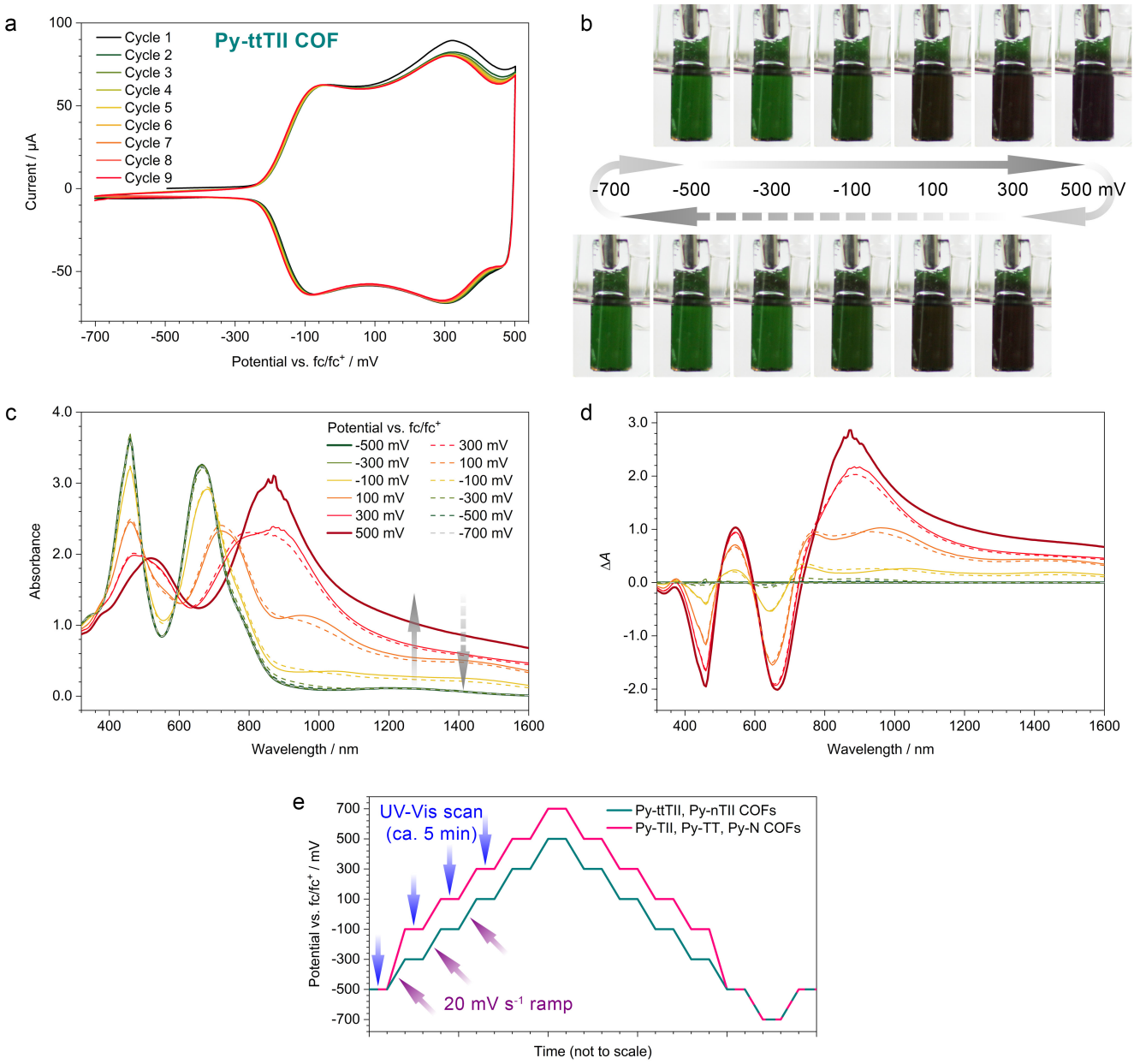

Figure S6-1. Electrochromic properties of the Py-ttTII COF. (**a**) Cyclic voltammetry scans of a COF film on ITO recorded at a scan rate of 20 mV s^{-1}. See the Methods section for experimental details. The Py-ttTII COF has two very well-defined oxidation waves at around -100 and +300 mV vs. fc/fc^+, respectively, and shows almost no drift over nine oxidation/reduction cycles. The stability of this COF over more oxidation/reduction cycles is analyzed in the next section.

(**b**) Photographs of the COF film taken during an oxidation (top row, left to right) / reduction (bottom row, right to left) cycle illustrating the electrochromic color changes.

(**c**) UV-Vis-NIR spectra recorded at different potentials using the ramp/dwell program shown in (**e**). The solid and dashed lines refer to spectra recorded at increasing (oxidation) and decreasing (reduction) potentials, respectively. The first oxidation step (+100 mV, orange line) produces a new absorption feature at 1000 nm, which is replaced by a strong absorption at 900 nm after the second oxidation step (+500 mV, dark red). The electrochromic color changes of the Py-ttTII COF are fully reversible with only minimal hysteresis (dashed lines). At -700 mV, the spectrum is indistinguishable from the initial spectrum (dashed grey line).

(**d**) Plot of the absorption difference between the oxidized COF and the initial spectrum. Oxidation of the Py-ttTII COF leads to the evolution of strong NIR absorption bands and a minor contribution at 550 nm, accompanied by two bleach bands at 450 and 650 nm.

(**e**) The voltage ramp programs used for the potential-dependent UV-Vis scans. Each UV-Vis scan (the first four scans are indicated by blue arrows) is followed by a 20 mV s^{-1} voltage ramp to the next potential (purple arrows). The larger-bandgap and/or more electron-deficient Py-TII, Py-TT and Py-N COFs require more positive potentials for oxidation. Hence, the potentials for the UV-Vis scans after the initial measurement are shifted by 200 mV (pink line).

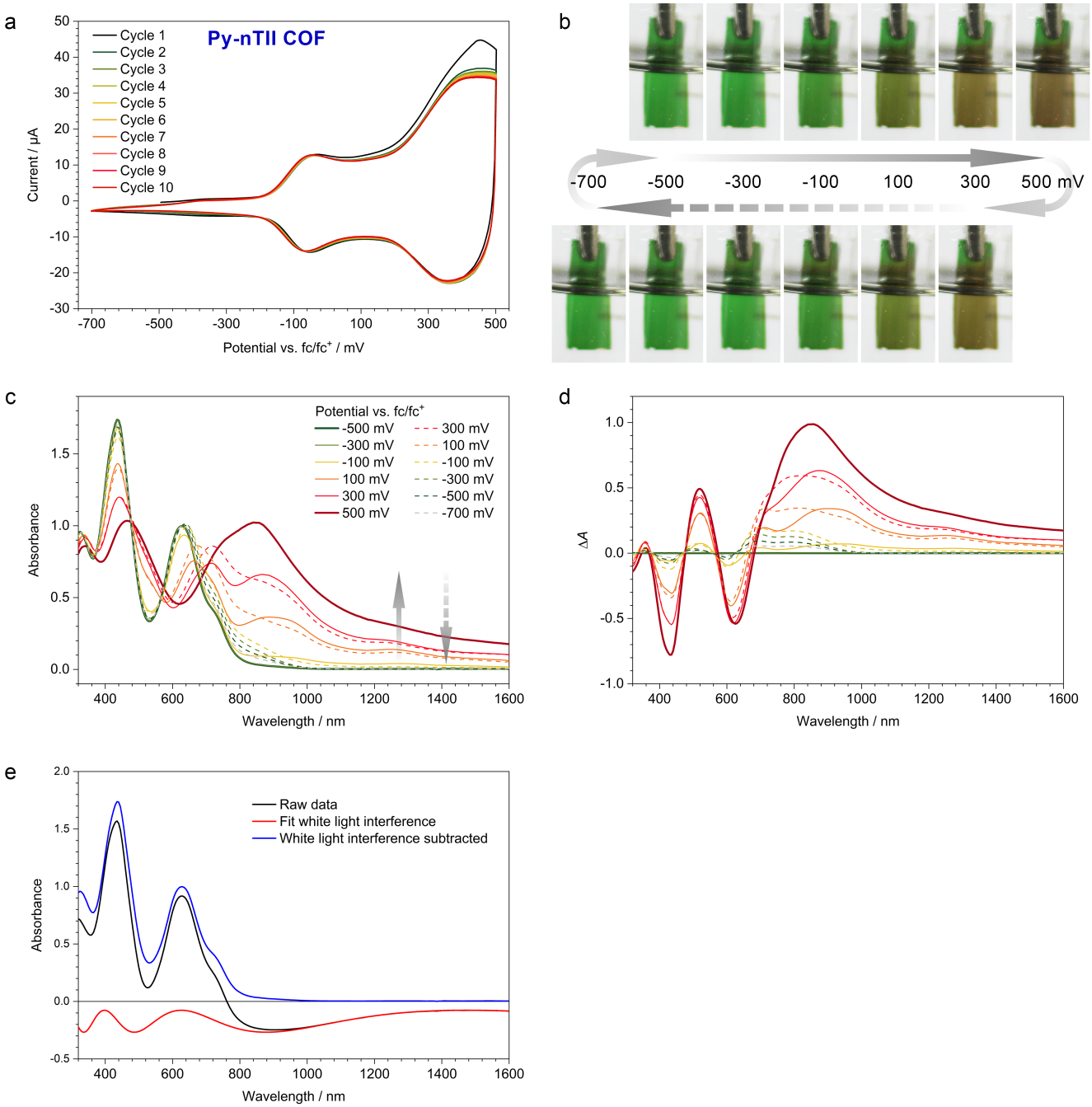

Figure S6-2. Electrochromic properties of the Py-nTII COF.

(**a**) Cyclic voltammetry scans of a COF film on a 10 nm Au/glass substrate, recorded at a scan rate of 20 mV s^{-1}. See the Methods section for experimental details. The Py-nTII COF has two very well-defined oxidation waves at around -50 and +350 mV vs. fc/fc^+, respectively, and shows almost no drift over ten oxidation/reduction cycles.

(**b**) Photographs of the COF film taken during an oxidation (top row, left to right) / reduction (bottom row, right to left) cycle illustrating the electrochromic color changes.

(**c**) UV-Vis-NIR spectra recorded at different potentials. The solid and dashed lines refer to spectra recorded at increasing (oxidation) and decreasing (reduction) potentials, respectively. The first oxidation step (+100 mV, orange line) produces a new absorption feature at 950 nm, which is replaced by a strong absorption at 900 nm after the second oxidation step (+500 mV, dark red line). The electrochromic color changes of the Py-nTII COF are almost fully reversible, however, with some hysteresis (dashed lines). At -700 mV, the spectrum follows the initial spectrum except for a minor residual absorption around 800 nm. The effect of white light interference, which is pronounced for this sample due to the Au substrate, was removed from the absorption spectra (see below).

(**d**) Plot of the absorption difference between the oxidized COF and the initial spectrum. Oxidation of the Py-nTII COF leads to the evolution of strong NIR absorption bands and a minor contribution at 550 nm, accompanied by two bleach bands at 450 and 650 nm.

(**e**) Background correction of the spectra. White light interference (red line) was approximated by the expression $A = 0.095 \cos(4\pi \cdot 544/\lambda + 1.64) - 0.176$ and subtracted from all spectra. For clarity, only the spectrum at -500 mV is displayed.

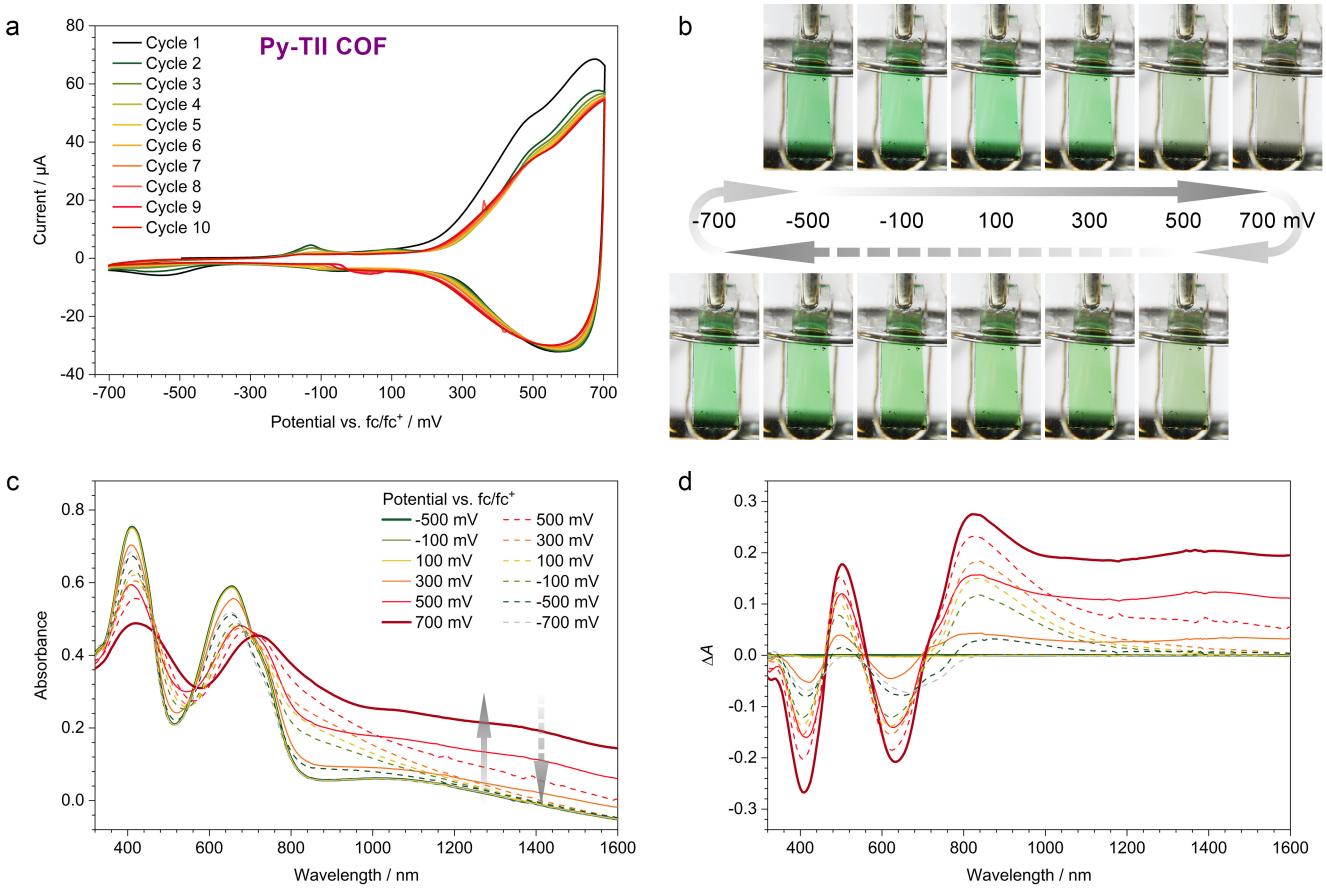

Figure S6-3. Electrochromic properties of the Py-TII COF.

(**a**) Cyclic voltammetry scans of a Py-TII COF film on ITO recorded at a scan rate of 20 mV s^{-1}. See the Methods section for experimental details. The Py-TII COF shows one oxidation wave at around +500 mV vs. fc/fc^+ and only moderate drift over ten oxidation/reduction cycles.

(**b**) Photographs of the COF film taken during an oxidation (top row, left to right) / reduction (bottom row, right to left) cycle illustrating the electrochromic color changes.

(**c**) UV-Vis-NIR spectra recorded at different potentials. The solid and dashed lines refer to spectra recorded at increasing (oxidation) and decreasing (reduction) potentials, respectively. Oxidation of the COF shifts the lowest-energy absorption band to about 800 nm and produces an additional very broad IR absorption that extends beyond the measurement range. In contrast to the COFs based on the larger and more electron-rich ttTII and nTII building blocks, the electrochromic color changes are not entirely reversible, probably due to pore blocking and a partial delamination of COF layers (see the manuscript for discussion).

(**d**) Plot of the absorption difference between the oxidized COF and the initial spectrum. Oxidation of the Py-TII COF leads to the evolution of strong NIR absorption bands and a minor contribution at 500 nm, accompanied by two bleach bands at 400 and 650 nm.

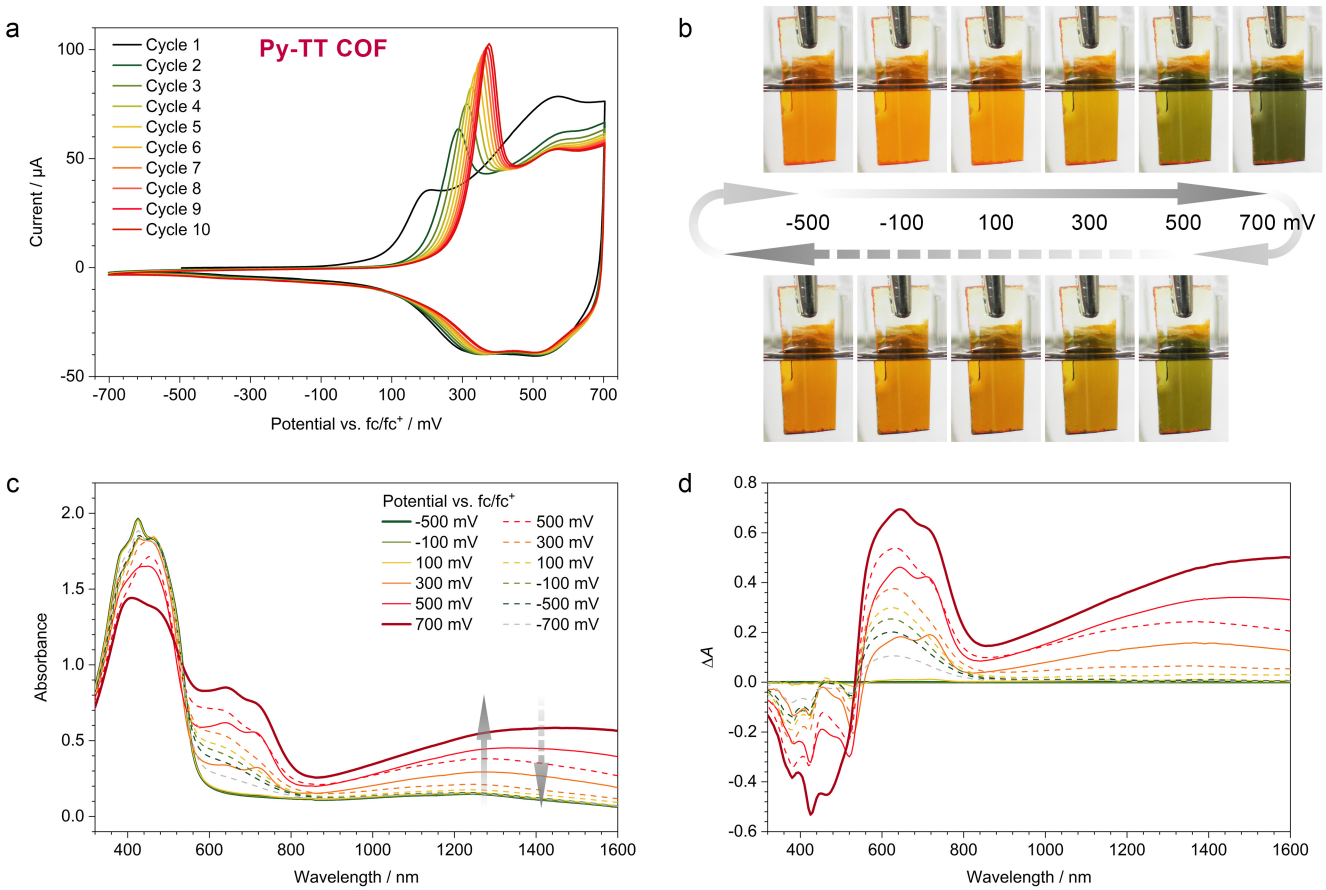

Figure S6-4. Electrochromic properties of the Py-TT COF.

(**a**) Cyclic voltammetry scans of a Py-TT COF film on ITO recorded at a scan rate of 20 mV s^{-1}. See the Methods section for experimental details. The Py-TT COF shows a well-defined oxidation wave at +200 mV during the first oxidation/reduction cycle, which shifts to higher potentials with every measurement cycle. We attribute this effect to limited diffusion of the electrolyte ions and a build-up of charged species in the considerably smaller pores of this COF (see the manuscript for discussion).

(**b**) Photographs of the COF film taken during an oxidation (top row, left to right) / reduction (bottom row, right to left) cycle illustrating the electrochromic color changes.

(**c**) UV-Vis-NIR spectra recorded at different potentials. The solid and dashed lines refer to spectra recorded at increasing (oxidation) and decreasing (reduction) potentials, respectively. Oxidation of the COF causes the evolution of two new absorption features between 600 and 800 nm as well as a broad IR absorption that extends beyond the measurement range. Unlike the large-pore Py-ttTII and Py-nTII COFs, the electrochromic color changes of the Py-TT COF are not entirely reversible, most likely due to pore blocking and a partial delamination of COF layers (see the manuscript for discussion).

(**d**) Plot of the absorption difference between the oxidized COF and the initial spectrum. Oxidation of the Py-TT COF leads to the evolution of a new absorption band between 600 and 800 nm that is accompanied by a bleach band around 400 nm.

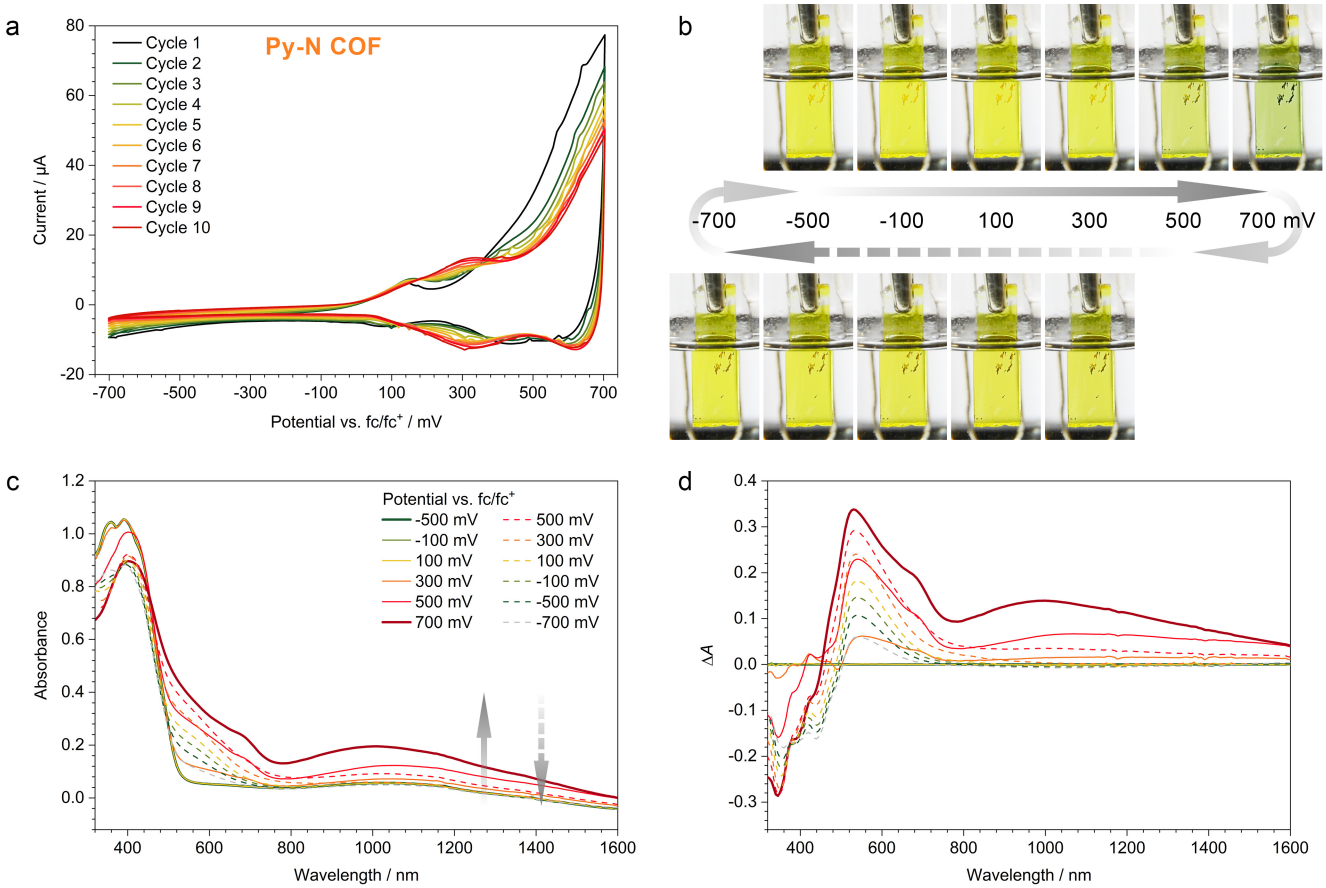

Figure S6-5. Electrochromic properties of the Py-N COF.

(**a**) Cyclic voltammetry scans of a Py-N COF film on ITO recorded at a scan rate of 20 mV s^{-1}. See the Methods section for experimental details. This COF shows an oxidation onset between 500 and 700 mV, which gradually shifts with every measurement cycle towards higher potentials. We attribute this effect to limited diffusion of the electrolyte ions and a build-up of charged species in the relatively small pores of this COF (see the manuscript for discussion). The small features at lower potentials are probably due to impurities or defects in the COF film.

(**b**) Photographs of the COF film taken during an oxidation (top row, left to right) / reduction (bottom row, right to left) cycle illustrating the electrochromic color changes.

(**c**) UV-Vis-NIR spectra recorded at different potentials. The solid and dashed lines refer to spectra recorded at increasing (oxidation) and decreasing (reduction) potentials, respectively. Oxidation of the COF causes the evolution of a new absorption feature around 600 nm as well as a broad IR absorption around 1000 nm. Unlike the large-pore Py-ttTII and Py-nTII COFs, the electrochromic color changes of the Py-N COF are not entirely reversible, most likely due to pore blocking and a partial delamination of COF layers (see the manuscript for discussion).

(**d**) Plot of the absorption difference between the oxidized COF and the initial spectrum. Oxidation of the Py-N COF leads to the evolution of a new absorption band around 600 nm that is accompanied by a bleach band around 380 nm.

H. Switching speed and stability

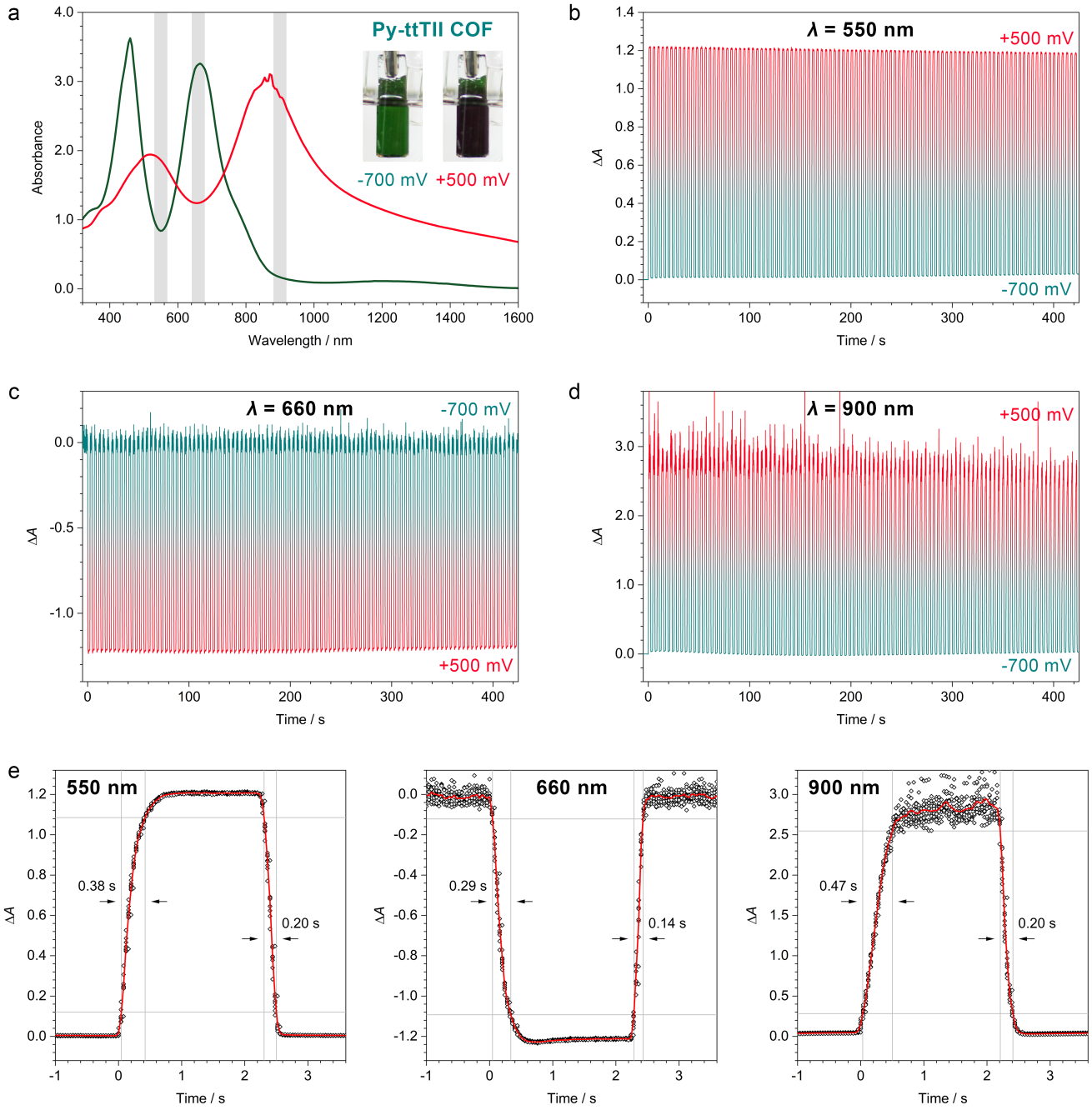

Figure S7-1. Electrochromic switching of the Py-ttTII COF. To avoid any "burn-in" effects, the switching experiments have been conducted with three freshly synthesized Py-ttTII COF samples from the same batch (one for each wavelength). Thus, time = 0 s corresponds to the first time that the samples are oxidized. Any differences between the Δ*A* values in (**a**) and (**b**)/(**c**)/(**d**) are due to slight variations in film thicknesses.

(**a**) Absorption spectra of a Py-ttTII COF film on ITO at -700 mV (green line) and +500 mV vs. fc/fc$^+$ (red line). The wavelengths used for the electrochromic switching experiments are indicated by grey lines. Insets: Photographs of the COF film.

(**b**) Electrochromic switching between the neutral and oxidized form of a Py-ttTII COF film over 100 cycles. The applied potential is switched between -700 and +500 mV vs. fc/fc$^+$ and held constant for 2 s after each potential step. The change of the absorbance is monitored at 550 nm. At this wavelength, the absorbance increases by 1.2 OD units upon oxidation with almost no degradation over 100 cycles. (**c**) Electrochromic switching over 100 cycles recorded at 660 nm. At this wavelength, the absorbance of the Py-ttTII COF is reduced by ca. 1.2 OD upon oxidation.

(**d**) Electrochromic switching over 100 cycles monitored at 900 nm. Upon oxidation, the absorbance increases by almost 3 OD.

(**e**) Switching speed of the Py-ttTII COF films in response to potential steps at 550 nm (left), 660 nm (middle) and 900 nm (right). The respective datasets (black dots) of the first ten switching cycles shown in (**b**)/(**c**)/(**d**) are averaged (red lines). The response is extremely fast with response times of 0.29 – 0.47 s (coloration) and 0.14 – 0.20 s (bleaching) between the 10% and 90% boundaries (grey lines).

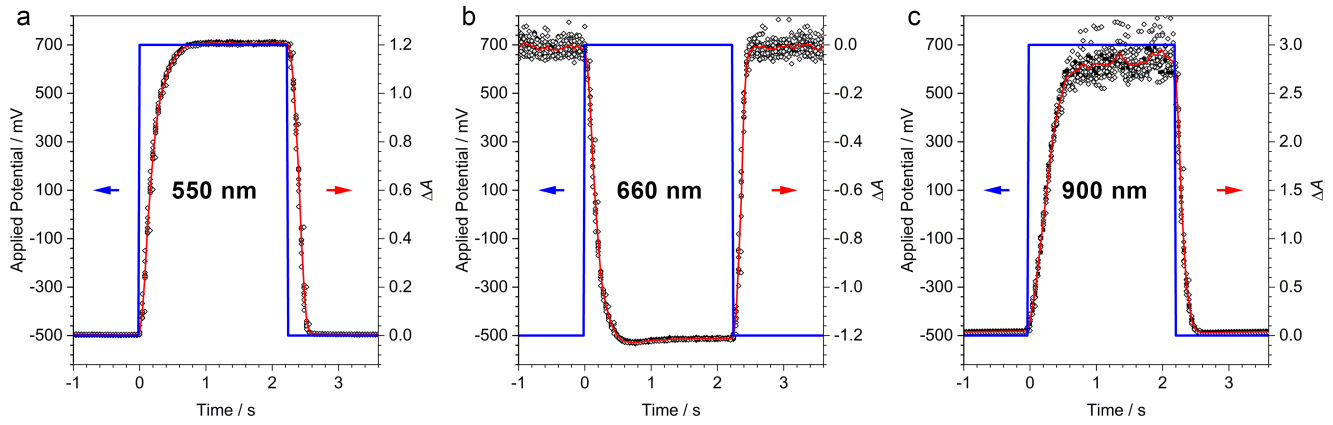

Figure S7-2. Overlay of the applied potential (blue, left *y*-axis) and the electrochromic response (black symbols and red line, right *y*-axis) of the Py-ttTII COF films at (**a**) 550 nm, (**b**) 660 nm, and (**c**) 900 nm.

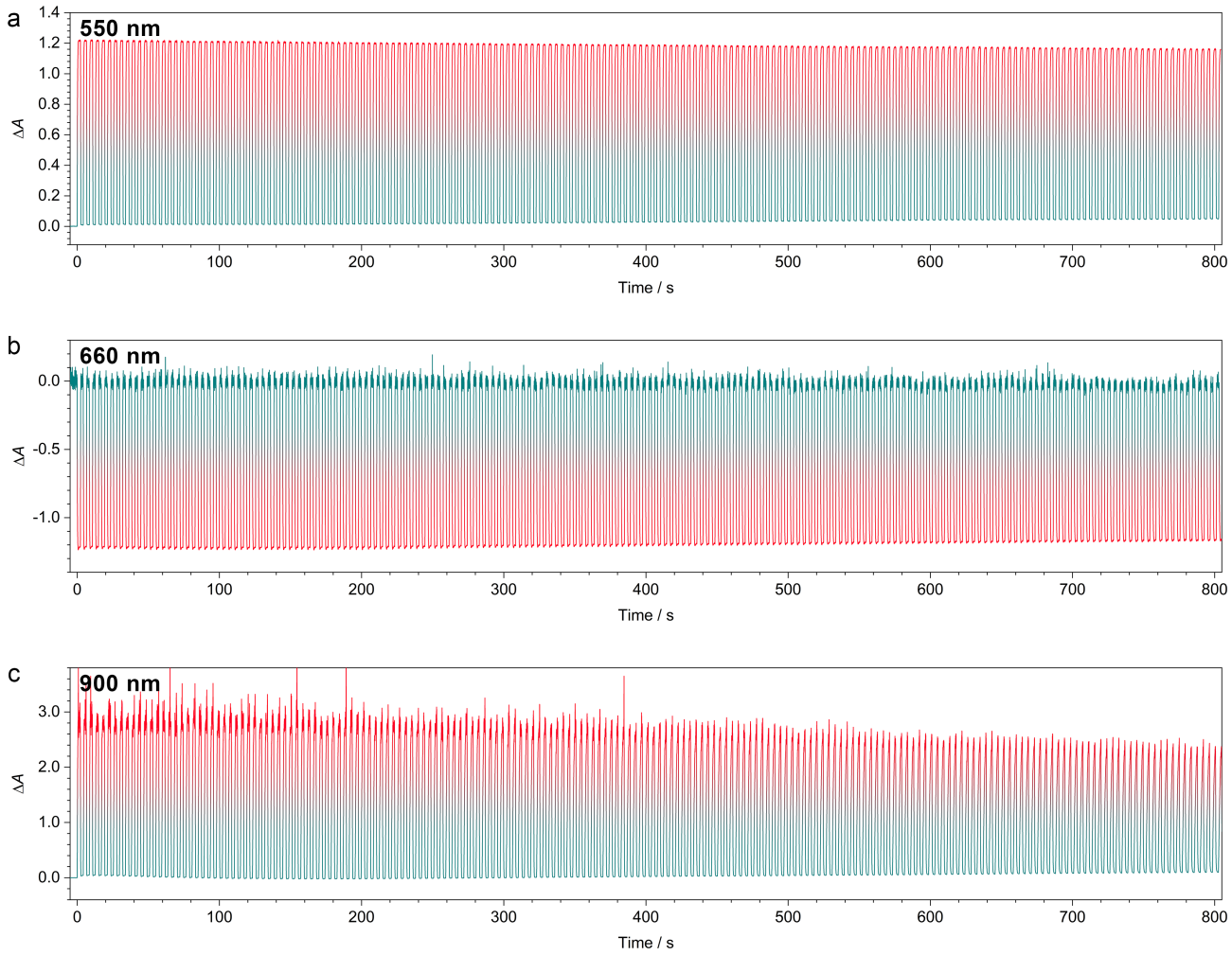

Figure S7-3. Electrochromic switching of the Py-ttTII COF over 200 cycles recorded at (**a**) 550 nm, (**b**) 660 nm, and (**c**) 900 nm. To avoid any "burn-in" effects, the switching experiments have been conducted with three freshly synthesized Py-ttTII COF samples from the same batch (one for each wavelength). Thus, time = 0 s corresponds to the first time that the samples are oxidized. The applied potential is switched between -700 and +500 mV vs. fc/fc^+ and held constant for 2 s after each potential step.

I. Coloration efficiency and extracted charge

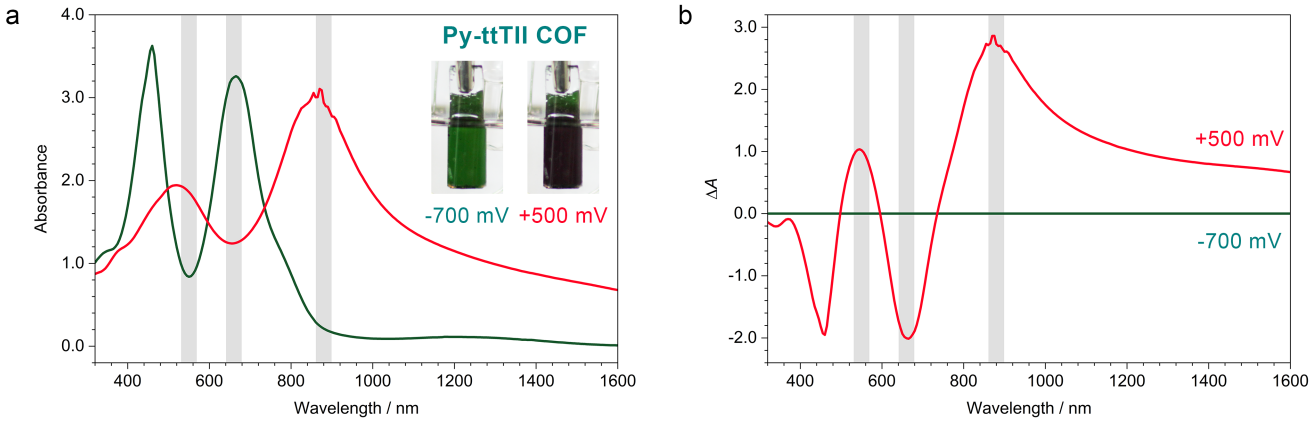

Figure S8. Spectra of the Py-ttTII COF in the neutral (green) and the 2x oxidized state (red). (**a**) Absorption spectra. (**b**) Absorption difference between the neutral and the oxidized COF. The wavelengths used for the calculation of the coloration efficiency are indicated by grey lines.

The electrochromic coloration efficiency (CE) relates the absorption change to the injected or extracted charge per unit area.

$$\mathrm{CE}(\lambda) = \frac{\Delta A(\lambda)}{Q/A}$$

ΔA is the absorption difference at the respective wavelength λ (Figure S8b).

ΔA(550 nm) = 1.03 ΔA(660 nm) = 2.01 ΔA(880 nm) = 2.78

A is the electrode area in contact with the electrolyte.

A = 11 mm × 6.3 mm = 0.69 cm^2

Q is the extracted charge, calculated from the oxidation scan shown in Figures 3b and S6-1a.

Q = 0.00223 C (0.00324 C cm^{-2}) for the two oxidation waves (-500 to +470 mV vs. fc/fc$^+$).

Using the above expression, the Py-ttTII COF has the following wavelength-dependent coloration efficiencies:

CE(550 nm) = 318 ± 32 cm^2 C^{-1} CE(660 nm) = 620 ± 62 cm^2 C^{-1} CE(880 nm) = 858 ± 86 cm^2 C^{-1}

These values are several times higher than the CEs of previous electrochromic COFs.[7-8]

How much charge is extracted per unit cell?

The 430 nm thick Py-ttTII COF film has a volume of 2.95 × 10^{-11} m^3 using the electrode dimensions stated above and assuming a pinhole-free film with 70% density due to its unique pillar-like morphology (Figure S5-1c). Using the refined unit cell parameters (V = 1.27 × 10^{-26} m^3), this relates to 1.63 × 10^{15} unit cells. Hence, the maximum charge that can be extracted by oxidation of every ttTII unit (the unit cell contains four) is

$$Q_{ox1} = 4Ne = 0.00104\ \mathrm{C}\ (0.00152\ \mathrm{C\ cm^{-2}})$$

$$Q_{ox2} = 4Ne \times 2 = 0.00209\ \mathrm{C}\ (0.00304\ \mathrm{C\ cm^{-2}})$$

N is the number of unit cells per film (corresponding to 4N ttTII units).

e is the elementary charge (1.602 × 10^{-19} C).

Q_{ox1} and Q_{ox2} refer to the one-electron and two-electron oxidation, respectively.

This calculation confirms our assignment of the two oxidation waves in the CV scans and the two distinct absorption spectra at different potentials to the one-electron and two-electron oxidation steps. The charge determined from the measured electrical current is slightly higher than the theoretical value, because there is a non-zero current flow through the electrochemical cell under applied bias.

Coloration efficiencies of the other COFs

$$\mathrm{CE}(\lambda) = \frac{\Delta A(\lambda)}{Q/A}$$

Py-nTII COF

ΔA(520 nm) = 0.490 ΔA(630 nm) = 0.547 ΔA(850 nm) = 0.992

A = 10 mm × 6.7 mm = 0.67 cm^2

Q = 0.000814 C (0.00122 C cm^{-2})

CE(520 nm) = 400 ± 60 cm^2 C^{-1} CE(630 nm) = 450 ± 70 cm^2 C^{-1} CE(850 nm) = 820 ± 120 cm^2 C^{-1}

Py-TII COF

ΔA(500 nm) = 0.179 ΔA(630 nm) = 0.208 ΔA(820 nm) = 0.275

A = 13 mm × 5.8 mm = 0.75 cm^2

Q = 0.00103 C (0.00137 C cm^{-2})

CE(500 nm) = 130 ± 20 cm^2 C^{-1} CE(630 nm) = 150 ± 20 cm^2 C^{-1} CE(820 nm) = 200 ± 30 cm^2 C^{-1}

Py-TT COF

ΔA(645 nm) = 0.692

A = 11 mm × 7.5 mm = 0.83 cm^2

Q = 0.00163 C (0.00198 C cm^{-2})

CE(645 nm) = 350 ± 35 cm^2 C^{-1}

Py-N COF

ΔA(530 nm) = 0.336

A = 12 mm × 6.5 mm = 0.78 cm^2

Q = 0.000738 C (0.000946 C cm^{-2})

CE(530 nm) = 360 ± 50 cm^2 C^{-1}

The CEs of the Py-ttTII and Py-nTII COFs, which are based on donor-acceptor-donor building blocks, are significantly higher than the CEs of the other frameworks, highlighting the importance of a suitable electronic design.

J. Building block syntheses

All reactions were performed in oven-dried glassware under argon atmosphere using standard Schlenk and glovebox techniques. Reagents and solvents were obtained in high-purity grades from commercial suppliers and were, unless shipped under argon, degassed and saturated with argon prior to use. Flash column chromatography was performed using silica gel (Acros Organics, 60 Å, 35 – 70 µm) and was continuously monitored via thin layer chromatography (TLC) using silica gel coated aluminum plates (Merck, 60 Å, F254).

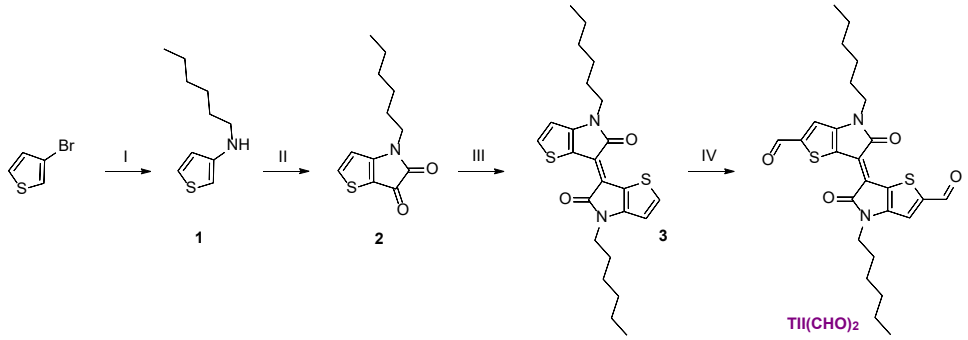

Figure S9. Syntheses of the hexyl-alkylated thienoisoindigo-core **3** and the $TII(CHO)_2$ building block. Reagents and conditions: (I) *n*-hexylamine, Cu, CuI, K_3PO_4, 2-dimethylaminoethanol, 80 °C, 65%. (II) oxalyl chloride, triethylamine, DCM, -15 °C/0°C/rt, 53%. (III) Lawesson's reagent, toluene, 100 °C, 5 min, 51%. (IV) LDA, DMF, THF, -78 °C/rt, 39%.

3-(hexylamino)thiophene (1)[6, 9]

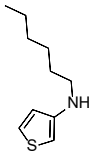

A reaction mixture containing 3-bromothiophene (12.2 g, 7.03 mL, 75.0 mmol, 1.0 eq.), *n*-hexylamine (11.4 g, 14.9 mL, 113 mmol, 1.5 eq.), copper powder (477 mg, 7.50 mmol, 10 mol%.), CuI (1.43 g, 7.50 mmol, 10 mol%) and K_3PO_4 (31.8 g, 150 mmol, 2.0 eq.) in anhydrous 2-dimethylaminoethanol (75 mL) were stirred under argon at 80 °C for 48 h. After cooling to room temperature, the supernatant was decanted and collected, and the solid residue was washed with anhydrous THF (4x 20 mL). The combined liquids were concentrated under reduced pressure. Purification via high vacuum distillation (10^{-2} mbar, 68 °C) yielded the title compound as a colorless and highly air-sensitive liquid (8.98 g, 49.0 mmol, 65%).

Due to the high air- and moisture-sensitivity, no NMR spectra were recorded and the product was used directly in the following step.

4-hexyl-4*H*-thieno[3,2-*b*]pyrrole-5,6-dione (2)

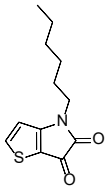

A solution of oxalyl chloride (9.95 g, 6.72 mL, 78.4 mmol, 1.6 eq.) in 49 mL of anhydrous DCM was cooled to -15 °C. Compound **1** (8.98 g, 49.0 mmol, 1.0 eq.) in 84 mL anhydrous DCM was slowly added via a syringe over 20 minutes under argon atmosphere. After the dropwise addition of triethylamine (14.9 g, 20.4 mL, 147 mmol, 3.0 eq.) at -15 °C, the resulting suspension was stirred for 1 h at 0 °C and allowed to warm to room temperature overnight. The reaction mixture was quenched with H_2O, and the product was extracted with DCM. The combined organic phases were washed with brine three times, dried over $MgSO_4$, and concentrated under reduced pressure. The product was purified by column chromatography (silica gel, DCM + 0.5% THF) to yield the title compound as a red oil (6.12 g, 25.8 mmol, 53%).

^{1}H-NMR (400 MHz, $CDCl_3$): 7.99 (d, *J* = 5.0 Hz, 1H), 6.78 (d, *J* = 5.0 Hz, 1H), 3.65 (t, *J* = 7.2 Hz, 2H), 1.73 – 1.61 (m, 2H), 1.41 – 1.24 (m, 6H), 0.88 (t, *J* = 7.1 Hz, 3H).

^{13}C-NMR (101 MHz, $CDCl_3$): 173.2, 165.3, 161.6, 144.0, 113.1, 111.2, 42.3, 31.5, 28.3, 26.6, 22.6, 14.1.

N,*N*'-dihexyl-thienoisoindigo (3)

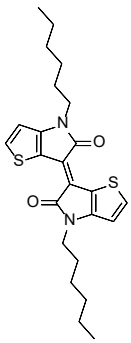

Compound **2** (4.68 g, 19.7 mmol, 2.0 eq.) was dissolved in 158 mL anhydrous toluene and added to Lawesson's reagent (3.99 g, 9.87 mmol, 1.0 eq.) under argon atmosphere at room temperature. In a preheated oil bath, the reaction mixture was stirred at 100 °C for 5 minutes. After cooling to room temperature, the product was concentrated under reduced pressure and all volatiles were removed under high vacuum. The crude product was purified by column chromatography (silica gel, DCM/*n*-hexane 2:1) to yield the title compound as a dark violet powder (2.23 g, 5.04 mmol, 51%).

^{1}H-NMR (400 MHz, $CDCl_3$): 7.53 (d, *J* = 5.2 Hz, 2H), 6.81 (d, *J* = 5.2 Hz, 2H), 3.80 (t, *J* = 7.3 Hz, 4H), 1.78 – 1.67 (m, 4H), 1.40 – 1.24 (m, 12H), 0.87 (t, *J* = 7.1 Hz, 6H).

^{13}C-NMR (101 MHz, $CDCl_3$): 171.1, 151.4, 134.5, 121.3, 114.3, 111.3, 42.0, 31.6, 28.7, 26.7, 22.7, 14.2.

5,5'-diformyl-*N*,*N*'-dihexyl-thienoisoindigo (TII(CHO)$_2$)

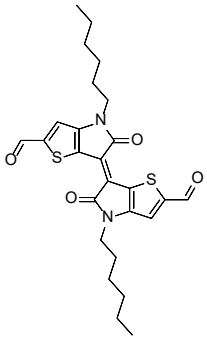

Following a literature procedure,[10] a solution of compound **3** (443 mg, 1.0 mmol, 1.0 eq.) in 40 mL anhydrous THF was added dropwise to a 1.0 M solution of LDA in THF/hexane (8.0 mmol, 8.0 eq.) cooled at -78 °C under argon atmosphere. The reaction mixture was stirred for 2 h at -78 °C. Anhydrous DMF (0.92 mL, 12 mmol, 12 eq.) was added dropwise and the resulting solution was stirred overnight, allowing the mixture to slowly warm to room temperature. The reaction was quenched with 100 mL of 0.5 M aqueous HCl, stirred for 1 h and extracted with DCM. The organic phase was washed with brine (2x), dried over $MgSO_4$ and concentrated under reduced pressure. The product was purified via column chromatography (silica gel, DCM + 2% EtOAc) to yield the title compound as an indigo blue solid (194 mg, 0.39 mmol, 39%).

^{1}H NMR (400 MHz, $CDCl_3$): 9.93 (s, 2H), 7.40 (s, 2H), 3.84 (t, *J* = 7.3 Hz, 4H), 1.80 – 1.70 (m, 4H), 1.42 – 1.26 (m, 12H), 0.89 (t, *J* = 7.1 Hz, 6H).

^{13}C NMR (101 MHz, $CDCl_3$): 183.0, 169.8, 152.3, 149.5, 123.8, 122.4, 115.1, 42.2, 31.5, 28.4, 26.7, 22.7, 14.1.

HR-EI-MS: *m*/*z* 498.16 (M^+, calculated for $C_{26}H_{30}N_2O_4S_2$: 498.16).

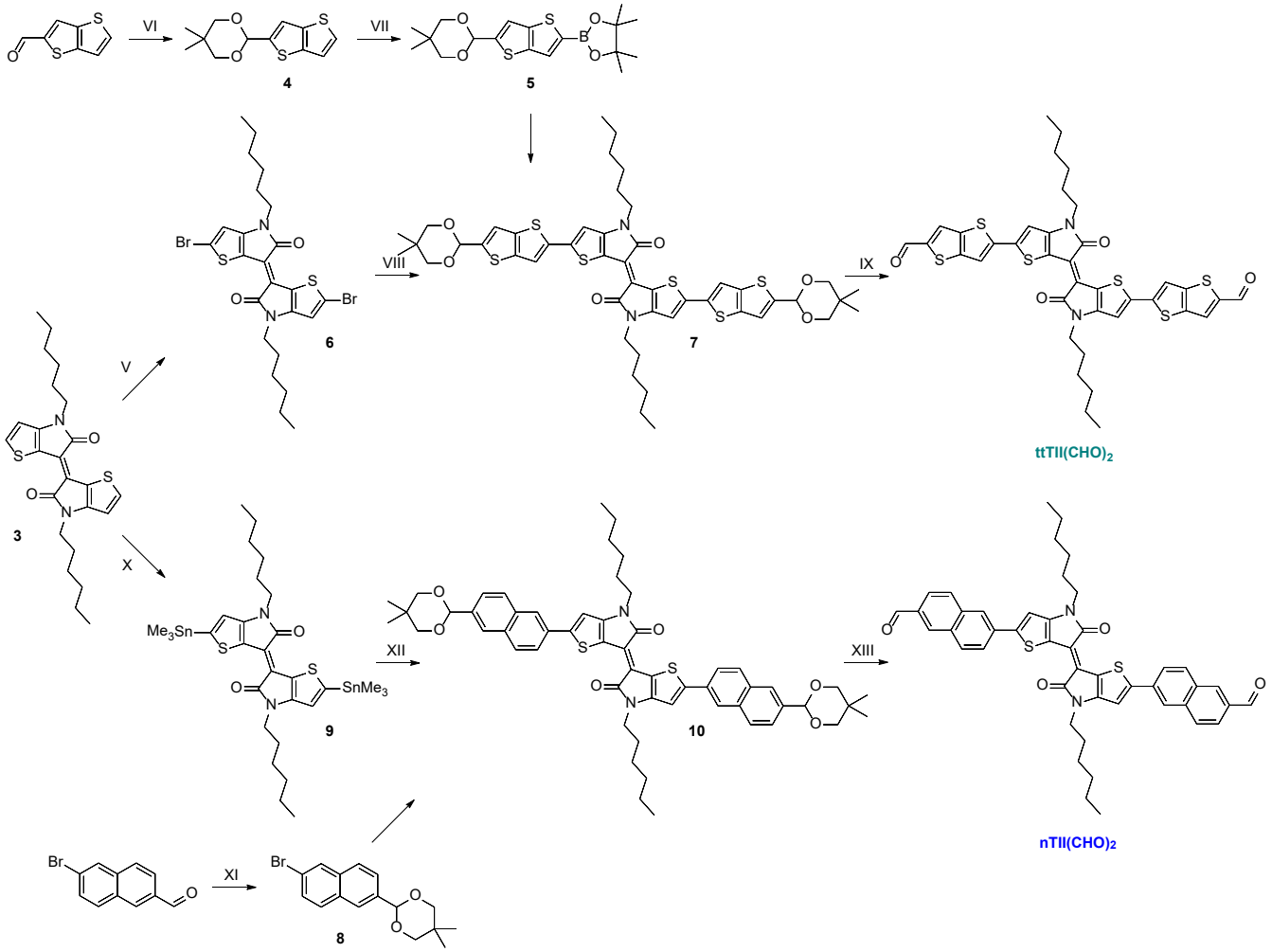

Figure S10. Syntheses of the new ttTII(CHO)$_2$ and nTII(CHO)$_2$ building blocks. Reagents and conditions: (V) NBS, THF, 0 °C, 84%. (VI) *p*-toluenesulfonic acid monohydrate, 2,2-dimethyl-1,3-propanediol, toluene, reflux, 97%. (VII) *n*-BuLi, 2-isopropoxy-4,4,5,5-tetramethyl-1,3,2-dioxaborolane, THF, -78 °C/rt, 58%. (VIII) $Pd_2(dba)_3$·$CHCl_3$, SPhos, K_2CO_3, *o*-xylene/H_2O, 100 °C, 74%. (IX) TFA, H_2O, rt, 76%. (X) LDA, Me_3SnCl, THF, -78 °C/rt, 83%. (XI) *p*-toluenesulfonic acid monohydrate, 2,2-dimethyl-1,3-propanediol, toluene, reflux, 83%. (XII) $Pd_2(dba)_3$, P(*o*-tol)$_3$, toluene, 110 °C, 84%. (XIII) TFA, H_2O, $CHCl_3$, rt, 81%.

5,5-dimethyl-2-(thieno[3,2-*b*]thiophen-2-yl)-1,3-dioxane (4)

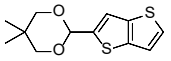

A reaction mixture containing thieno[3,2-*b*]thiophene-2-carboxaldehyde (1000 mg, 5.94 mmol, 1.0 eq.), 2,2-dimethyl-1,3-propanediol (1175 mg, 11.3 mmol, 1.9 eq.) and *p*-toluenesulfonic acid monohydrate (91.3 mg, 0.48 mmol, 8 mol%) in 59 mL toluene was refluxed at 110 °C for 2.5 h. After cooling to room temperature, the reaction mixture was poured into water, extracted with DCM and washed with brine (3x). The organic phase was dried over $MgSO_4$ and concentrated under reduced pressure. Purification via column chromatography (silica gel, DCM/*n*-hexane 3:2) yielded the title compound as a white powder (1468 mg, 5.77 mmol, 97%).

^{1}H NMR (400 MHz, $CDCl_3$): 7.35 (d, *J* = 5.2 Hz, 1H), 7.32 (s, 1H), 7.24 (d, *J* = 5.3 Hz, 1H), 5.68 (s, 1H), 3.78 (d, *J* = 11.3 Hz, 2H), 3.66 (d, *J* = 10.8 Hz, 2H), 1.29 (s, 3H), 0.81 (s, 3H).

^{13}C NMR (101 MHz, $CDCl_3$): 143.4, 139.4, 138.5, 127.5, 119.7, 117.7, 98.5, 77.7, 30.4, 23.1, 22.0.

2-(5-(5,5-dimethyl-1,3-dioxan-2-yl)thieno[3,2-*b*]thiophen-2-yl)-4,4,5,5-tetramethyl-1,3,2-dioxaborolane (5)

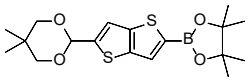

Compound **4** (715 mg, 2.81 mmol, 1.0 eq.) was dissolved in 23.5 mL THF and cooled to -78 °C. *n*-BuLi (2.0 M in cyclohexane, 4.22 mmol, 1.5 eq.) was added dropwise and the solution was stirred for 1.5 h at -78 °C. Subsequently, 2-isopropoxy-4,4,5,5-tetramethyl-1,3,2-dioxaborolane (785 mg, 0.86 mL, 4.22 mmol, 1.5 eq.) was added and the reaction mixture was stirred for 1 h at -78 °C. The resulting suspension was allowed to warm to room temperature and stirred overnight. The reaction was quenched with H_2O (25 mL) and stirred for 15 minutes. The product was extracted with diethyl ether and washed with brine three times. The organic phase was dried over $MgSO_4$ and concentrated under reduced pressure. The product was purified via recrystallization from *n*-hexane (75 mL, 70 °C to room temperature), collected by filtration and dried under high vacuum to yield the title compound as colorless needles (612 mg, 1.61 mmol, 58%).

^{1}H NMR (400 MHz, $CDCl_3$): 7.73 (s, 1H), 7.33 (s, 1H), 5.68 (s, 1H), 3.78 (d, *J* = 11.3 Hz, 2H), 3.66 (d, *J* = 10.7 Hz, 2H), 1.35 (s, 12H), 1.28 (s, 3H), 0.81 (s, 3H).

5,5'-dibromo-*N*,*N*'-dihexyl-thienoisoindigo (6)

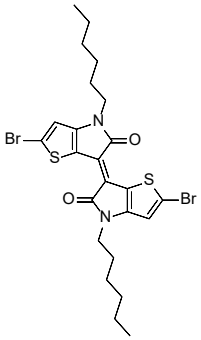

A solution of compound **3** (2230 mg, 5.04 mmol, 1.0 eq.) in 231 mL anhydrous THF was cooled to 0 °C. *N*-Bromosuccinimide (1883 mg, 10.6 mmol, 2.1 eq.) was added and the reaction mixture was stirred for 1.5 h at 0 °C in the dark. The reaction was quenched with H_2O, extracted with $CHCl_3$, and washed with brine (2x). The organic phase was dried over $MgSO_4$ and concentrated under reduced pressure. Purification via column chromatography (silica gel, $CHCl_3$/cyclohexane 1:1) yielded the title compound as a dark blue powder (2547 mg, 4.24 mmol, 84%).

^{1}H NMR (400 MHz, $CDCl_3$): 6.84 (s, 2H), 3.74 (t, *J* = 7.3 Hz, 4H), 1.75 – 1.63 (m, 4H), 1.40 – 1.24 (m, 12H), 0.88 (t, *J* = 7.1 Hz, 6H).

^{13}C NMR (101 MHz, $CDCl_3$): 170.2, 150.0, 123.4, 119.9, 115.0, 114.8, 42.0, 31.6, 28.7, 26.7, 22.7, 14.2.

5,5'-bis(5-(5,5-dimethyl-1,3-dioxane-2-yl)thienothiophen-2-yl)-*N*,*N*'-dihexyl-thienoisoindigo (7)

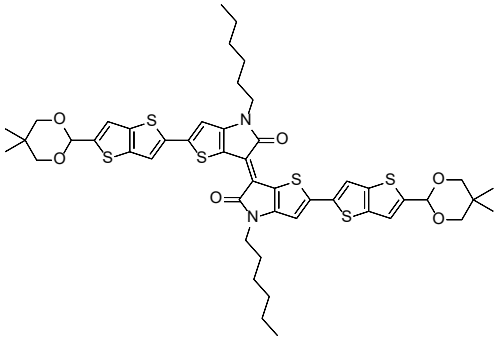

A reaction mixture containing compound **6** (143 mg, 0.24 mmol, 1.0 eq.), compound **5** (217 mg, 0.57 mmol, 2.4 eq.), $Pd_2(dba)_3{\cdot}CHCl_3$ (24.6 mg, 0.024 mmol, 10 mol%), SPhos (19.5 mg, 0.05 mmol, 20 mol%), and K_2CO_3 (132 mg, 0.95 mmol, 4 eq.) in 7.6 mL *o*-xylene and 1.9 mL H_2O was stirred at 100 °C for 20 h under argon atmosphere. After cooling to room temperature, the mixture was poured into water and extracted with DCM. The organic phase was dried over $MgSO_4$ and concentrated under reduced pressure. Purification by column chromatography (silica gel, DCM) yielded the title compound as a dark green powder (168 mg, 0.18 mmol, 74%).

^{1}H NMR (400 MHz, $CDCl_3$): 7.53 (s, 2H), 7.29 (s, 2H), 6.91 (s, 2H), 5.68 (s, 2H), 3.86 – 3.75 (m, 8H), 3.67 (d, *J* = 11.0 Hz, 4H), 1.80 – 1.70 (m, 4H), 1.45 – 1.31 (m, 12H), 1.29 (s, 6H), 0.89 (t, *J* = 7.1 Hz, 6H), 0.82 (s, 6H).

5,5'-bis(2-formylthienothiophen-5-yl)-*N*,*N*'-dihexyl-thienoisoindigo (ttTII(CHO)$_2$)

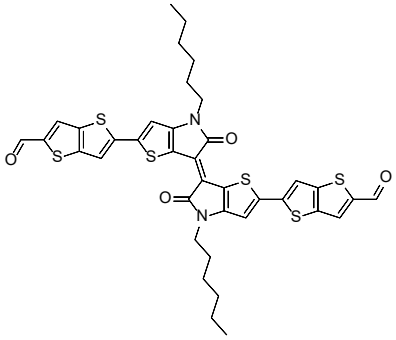

To a solution of compound **7** (160 mg, 0.17 mmol, 1.0 eq.) dissolved in 25 mL $CHCl_3$, trifluoroacetic acid (5 mL) and H_2O (0.5 mL) were added dropwise and left to stir at room temperature for 4 h under argon atmosphere. The reaction mixture was slowly added into saturated aqueous $NaHCO_3$ (100 mL) and extracted with $CHCl_3$. The combined organic phase was washed with brine, dried over $MgSO_4$ and concentrated to about 100 mL under reduced pressure. The product was precipitated by addition of MeOH (100 mL), collected by filtration, washed with $CHCl_3$ (20 mL) and dried under high vacuum to yield the title compound as a dark green powder (99 mg, 0.13 mmol, 76%).

^{1}H NMR (400 MHz, $CDCl_3$): 9.96 (s, 2H), 7.90 (s, 2H), 7.59 (s, 2H), 7.01 (s, 2H), 3.85 (t, *J* = 7.4 Hz, 4H), 1.83 – 1.73 (m, 4H), 1.41 – 1.29 (m, 12H), 0.90 (t, *J* = 7.0 Hz, 6H).

HR-EI-MS: *m*/*z* 774.08 (M^+, calculated for $C_{38}H_{34}N_2O_4S_6$: 774.08).

2-(6-bromonaphthalen-2-yl)-5,5-dimethyl-1,3-dioxane (8)

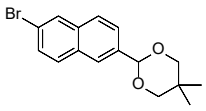

A reaction mixture containing 6-bromo-2-naphthaldehyde (500 mg, 2.1 mmol, 1.0 eq.), *p*-toluenesulfonic acid monohydrate (32.3 mg, 0.17 mmol, 8 mol%) and 2,2-dimethyl-1,3-propanediol (421 mg, 4.0 mmol, 1.9 eq.) in anhydrous toluene (21 mL) were refluxed at 110 °C for 2.5 h under argon atmosphere. After cooling to room temperature, the reaction mixture was poured into water, extracted with DCM and washed with brine (3x). The organic phase was dried over $MgSO_4$, concentrated under reduced pressure, and purified via column chromatography (silica gel, DCM/cyclohexane 1:1) to yield the title compound as a white powder (589 mg, 1.83 mmol, 86%).

^{1}H NMR (400 MHz, $CDCl_3$): 8.00 (s, 1H), 7.95 (s, 1H), 7.79 – 7.70 (m, 4H), 7.65 (dd, *J* = 8.5, 1.7 Hz, 1H), 7.54 (dd, *J* = 8.7, 2.0 1H), 5.54 (s, 1H), 3.82 (d, *J* = 11.3, 2H), 3.72 (d, *J* = 10.6, 2H), 1.33 (s, 3H), 0.83 (s, 3H).

^{13}C NMR (101 MHz, $CDCl_3$): 136.6, 134.8, 131.6, 130.2, 129.9, 129.6, 127.4, 125.6, 125.1, 120.4, 101.7, 30.5, 27.1, 23.3, 22.1.

5,5'-bis(trimethylstannyl)-*N*,*N*'-dihexyl-thienoisoindigo (9)[10]

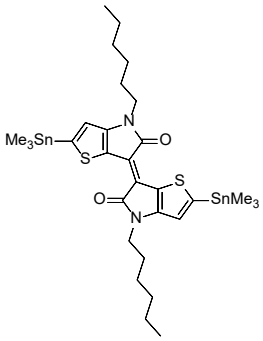

Compound **3** (443 mg, 1.0 mmol, 1 eq.) was dissolved in 50 mL anhydrous THF and added dropwise to LDA (1.0 M in THF/hexane, 8.0 mmol, 8.0 eq.) precooled to -78 °C under argon atmosphere. After stirring for 2 h at this temperature, Me_3SnCl (1.0 M in THF, 12 mmol, 12.0 eq.) was added and the reaction mixture was allowed to slowly warm to room temperature overnight. The reaction was quenched with H_2O and all volatiles were removed under high vacuum at 70 °C. The residue was dissolved in DCM, washed with brine (3x), dried over $MgSO_4$, and the solvent was removed under reduced pressure. The product was washed with MeOH (200 mL), filtrated and dried under high vacuum to yield the title compound as a purple powder (639 mg, 0.83 mmol, 83%).

^{1}H NMR (400 MHz, $CDCl_3$): 6.83 (s, 2H), 3.81 (t, *J* = 7.4 Hz, 4H), 1.79 – 1.68 (m, 4H), 1.42 – 1.24 (m, 12H), 0.88 (t, *J* = 7.1 Hz, 6H), 0.43 (s, with Sn coupling, 18H).

^{13}C NMR (101 MHz, $CDCl_3$): 171.8, 152.5, 151.1, 120.4, 120.2, 117.8, 42.0, 31.7, 28.8, 26.8, 22.7, 14.2, -7.9.

5,5'-bis(6-(5,5-dimethyl-1,3-dioxane-2-yl)naphthalen-2-yl)-*N*,*N*'-dihexyl-thienoisoindigo (10)

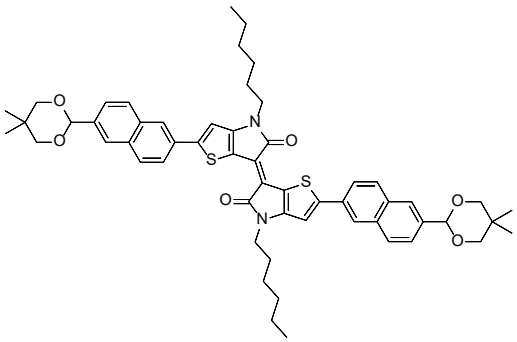

A reaction mixture containing compound **9** (230 mg, 0.3 mmol, 1.0 eq.), compound **8** (212 mg, 0.66 mmol, 2.2 eq.), $Pd_2(dba)_3$ (13.7 mg, 0.015 mmol, 5 mol%) and tri(*o*-tolyl)phosphine (36.5 mg, 0.12 mmol, 0.4 eq.) in 10 mL anhydrous toluene was heated to 110 °C for 4 d. After cooling to room temperature, all volatiles were removed under high vacuum at 60 °C. The solid residue was dissolved in DCM and purified by column chromatography (silica gel, DCM) to yield the title compound as a blue-green powder (234 mg, 0.25 mmol, 84%).

^{1}H NMR (400 MHz, $CDCl_3$): 8.22 (s, 2H), 7.96 (s, 2H), 7.91 – 7.81 (m, 6H), 7.67 (dd, *J* = 8.5, 1.7 Hz, 2H), 7.17 (s, 2H), 5.56 (s, 2H), 3.89 (t, *J* = 7.3 Hz, 4H), 3.84 (d, *J* = 11.2 Hz, 4H), 3.72 (d, *J* = 10.9 Hz, 4H), 1.88 – 1.77 (m, 4H), 1.42 – 1.29 (m, 18H), 0.91 (t, *J* = 7.1 Hz, 6H), 0.85 (s, 6H).

5,5'-bis(2-formylnaphthalen-6-yl)-*N*,*N*'-dihexyl-thienoisoindigo (nTII(CHO)$_2$)

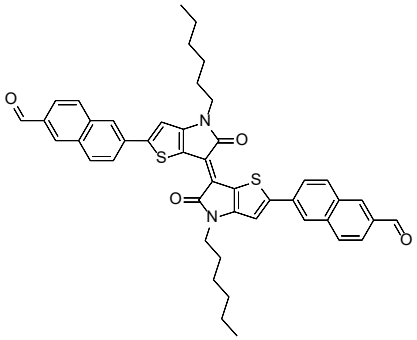

To a solution of compound **10** (572 mg, 0.62 mmol, 1.0 eq.) dissolved in 60 mL $CHCl_3$, trifluoroacetic acid (12 mL) and H_2O (1.2 mL) were added dropwise and left to stir at room temperature for 4 h under argon atmosphere. The reaction was neutralized by the dropwise addition into saturated aqueous $NaHCO_3$ (150 mL) and extracted with $CHCl_3$. The product was precipitated by the addition of MeOH (50 mL), collected by filtration, and washed with H_2O (200 mL), acetone (30 mL) and $CHCl_3$ (20 mL). Drying under high vacuum yielded the title compound as a dark green powder (375 mg, 0.50 mmol, 81%).

^{1}H NMR (400 MHz, $CDCl_3$): 10.15 (s, 2H), 8.30 (s, 2H), 8.25 (s, 2H), 8.03 – 7.90 (m, 8H), 7.24 (s, 2H), 3.90 (t, *J* = 7.3 Hz, 4H), 1.87 – 1.77 (m, 4H), 1.42 – 1.28 (m, 12H), 0.91 (t, *J* = 7.0 Hz, 6H).

HR-EI-MS: *m*/*z* 750.26 (M^+, calculated for $C_{46}H_{42}N_2O_4S_2$: 750.26).

K. NMR spectra of the TII building blocks

^{1}H and ^{13}C NMR spectra. Residual (undeuterated) solvent peaks and H_2O/HDO are marked with asterisks.

TII(CHO)$_2$

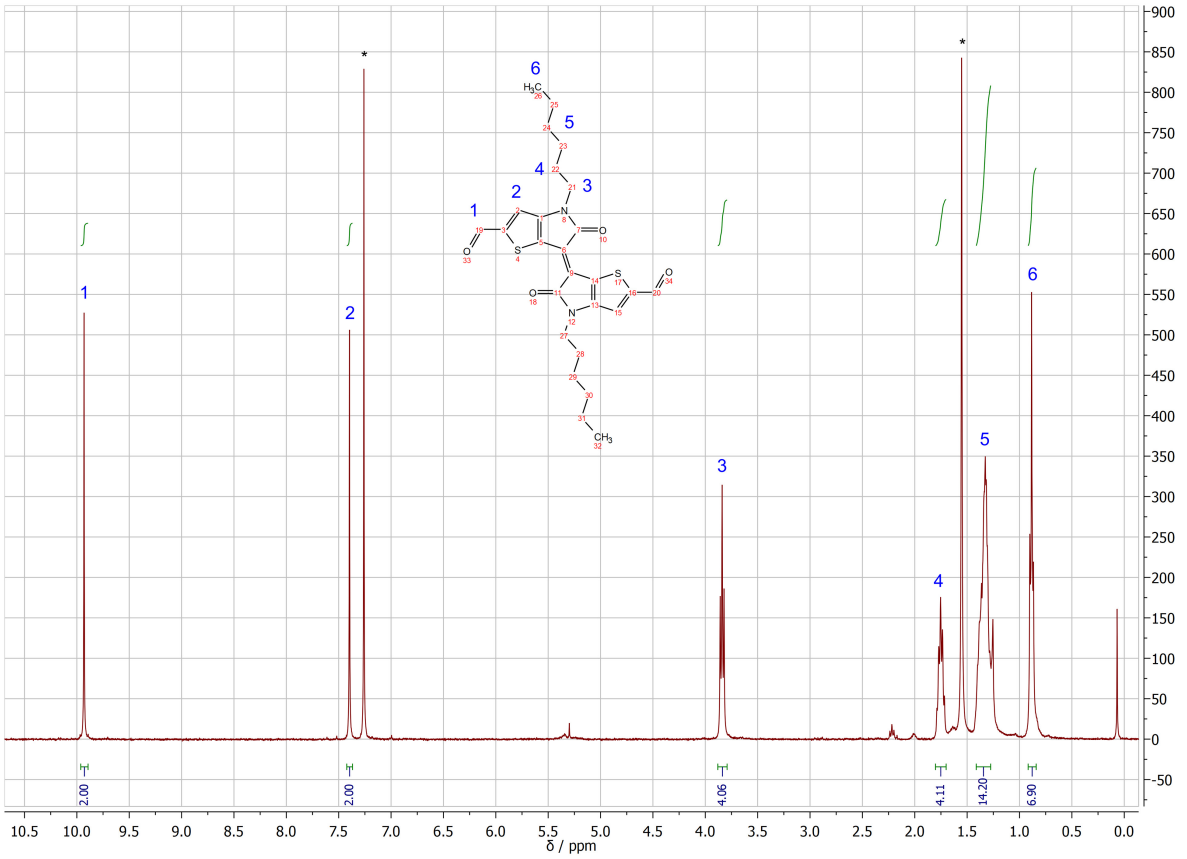

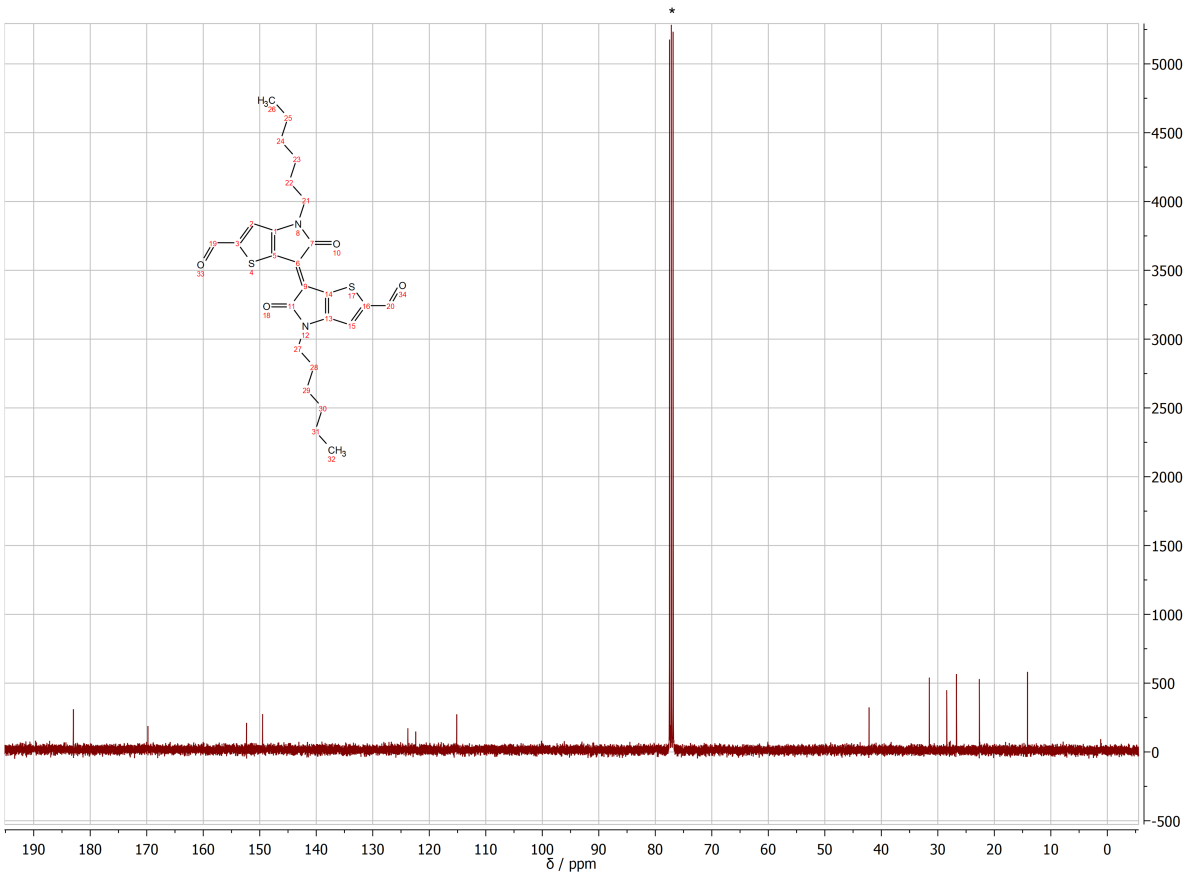

ttTII(CHO)$_2$

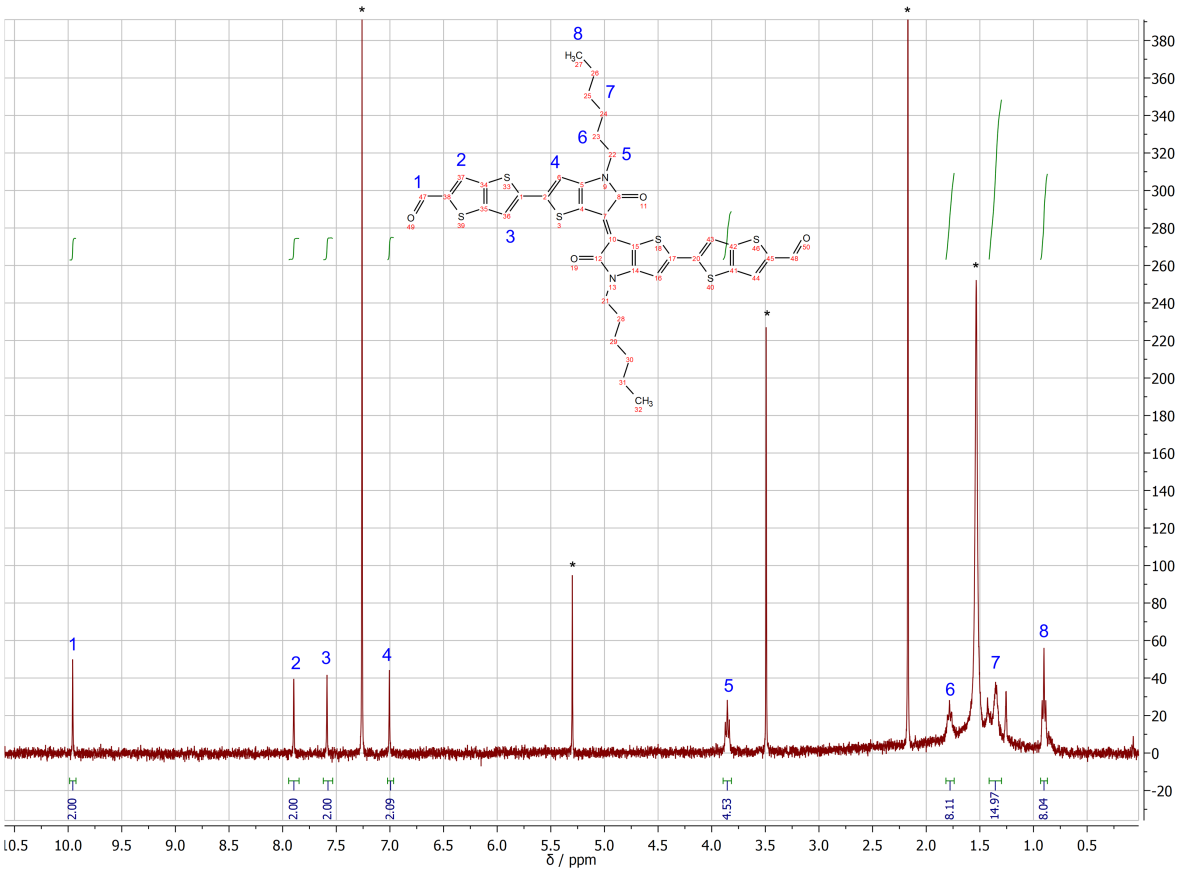

nTII(CHO)$_2$

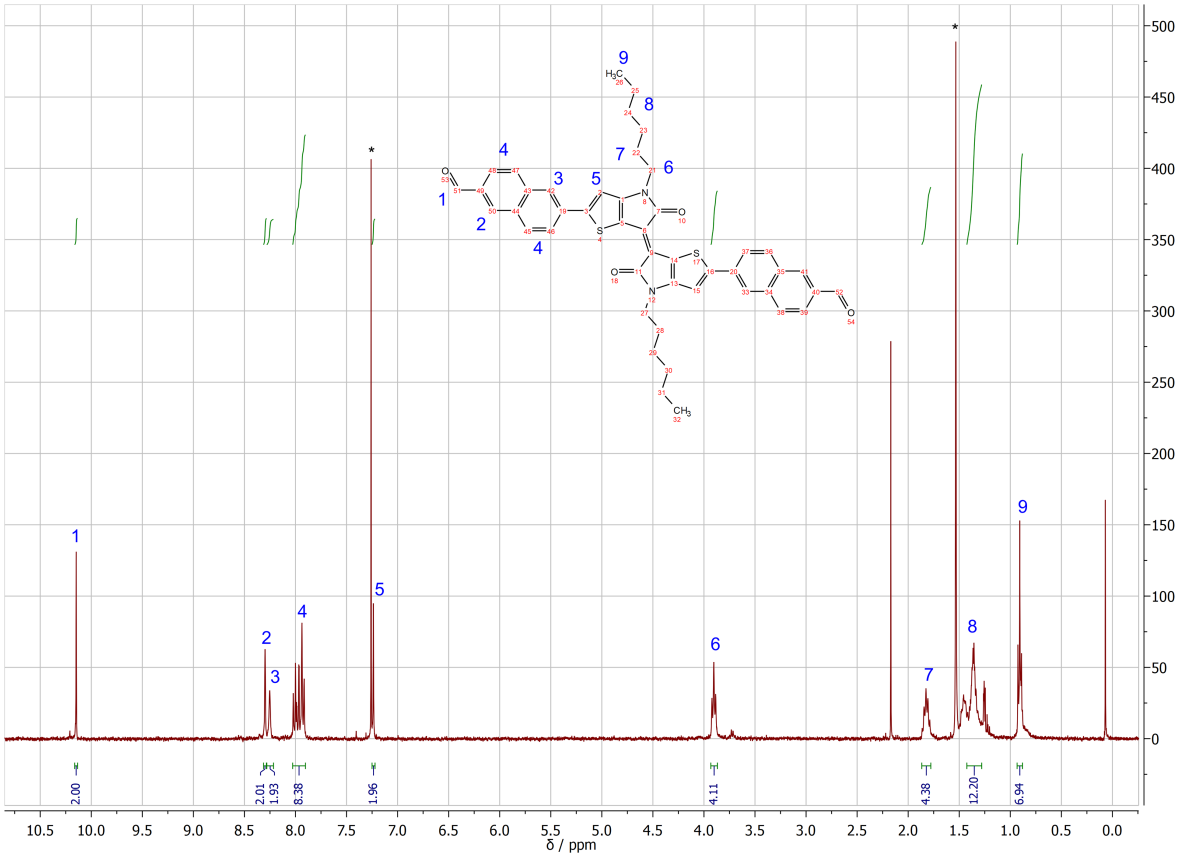

L. Solid-state NMR spectra

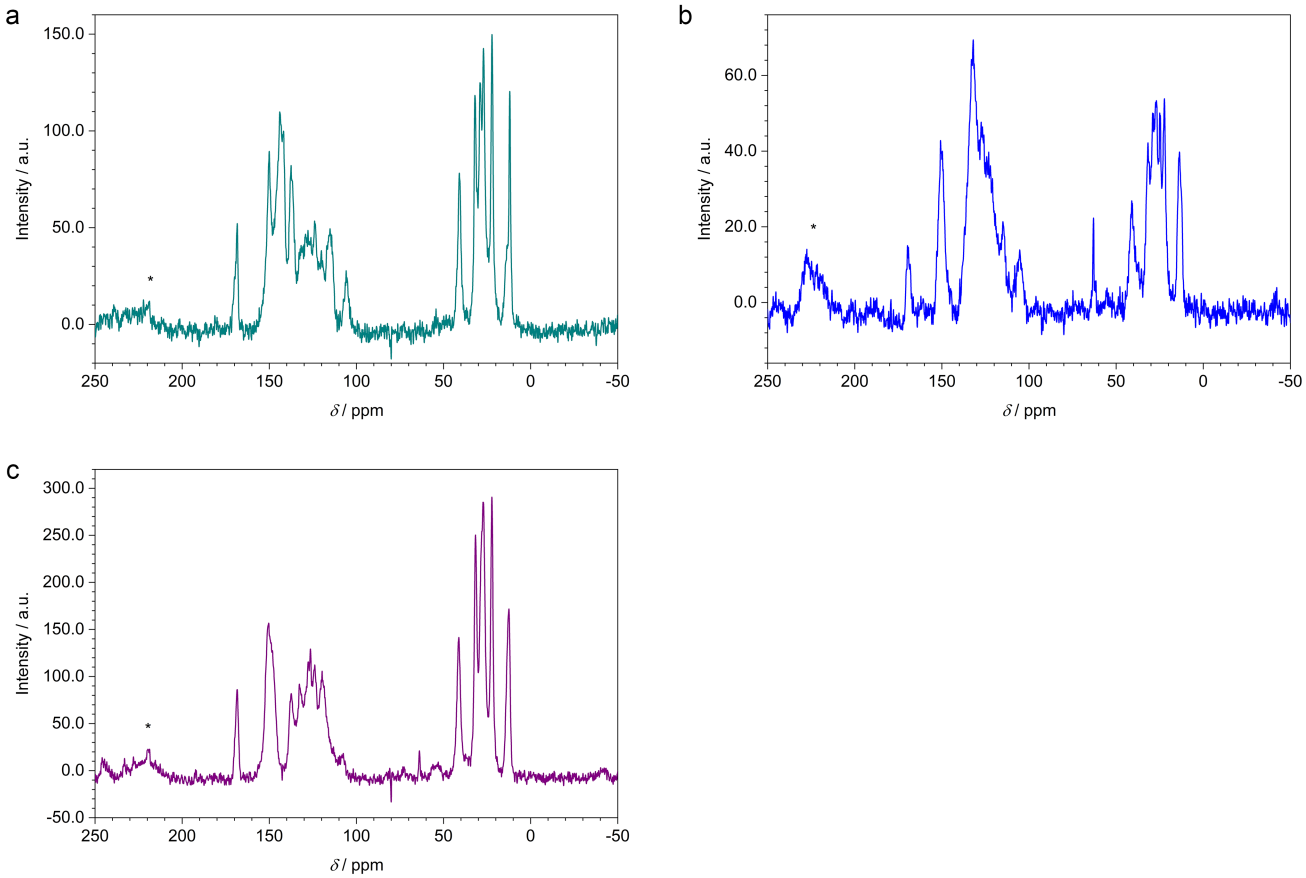

Figure S11. Solid-state ^{13}C cross-polarization magic angle spinning (CP-MAS) NMR spectra of the thienoisoindigo COFs. (**a**) Py-ttTII COF, (**b**) Py-nTII COF, (**c**) Py-TII COF. The appearance of the characteristic imine C=N resonance at around 170 ppm and the absence of residual aldehyde signals around 190 ppm confirm the successful COF formation.[11] The signals in the 100-150 ppm range originate from the (hetero)aromatic framework backbone, while the six well-resolved signals below 50 ppm are due to the hexyl chains. Spinning sidebands are marked with asterisks.

M. References

[1] T. Düren, F. Millange, G. Férey, K. S. Walton, R. Q. Snurr, *J. Phys. Chem. C* **2007**, *111*, 15350.

[2] F. Auras, L. Ascherl, A. H. Hakimioun, J. T. Margraf, F. C. Hanusch, S. Reuter, D. Bessinger, M. Döblinger, C. Hettstedt, K. Karaghiosoff, S. Herbert, P. Knochel, T. Clark, T. Bein, *J. Am. Chem. Soc.* **2016**, *138*, 16703.

[3] L. Ascherl, E. W. Evans, J. Gorman, S. Orsborne, D. Bessinger, T. Bein, R. H. Friend, F. Auras, *J. Am. Chem. Soc.* **2019**, *141*, 15693.

[4] L. Ascherl, E. W. Evans, M. Hennemann, D. Di Nuzzo, A. G. Hufnagel, M. Beetz, R. H. Friend, T. Clark, T. Bein, F. Auras, *Nat. Commun.* **2018**, *9*, 3802.

[5] M. Calik, F. Auras, L. M. Salonen, K. Bader, I. Grill, M. Handloser, D. D. Medina, M. Dogru, F. Löbermann, D. Trauner, A. Hartschuh, T. Bein, *J. Am. Chem. Soc.* **2014**, *136*, 17802.

[6] D. Bessinger, L. Ascherl, F. Auras, T. Bein, *J. Am. Chem. Soc.* **2017**, *139*, 12035.

[7] Q. Hao, Z.-J. Li, C. Lu, B. Sun, Y.-W. Zhong, L.-J. Wan, D. Wang, *J. Am. Chem. Soc.* **2019**, *141*, 19831.

[8] F. Yu, W. Liu, S.-W. Ke, M. Kurmoo, J.-L. Zuo, Q. Zhang, *Nat. Commun.* **2020**, *11*, 5534.

[9] Y. Koizumi, M. Ide, A. Saeki, C. Vijayakumar, B. Balan, M. Kawamotoa, S. Seki, *Polym. Chem.* **2013**, *4*, 484.

[10] T. Hasegawa, M. Ashizawa, J. Hiyoshi, S. Kawauchi, J. Mei, Z. Bao, H. Matsumoto, *Polym. Chem.* **2016**, *7*, 1181.

[11] H. L. Nguyen, C. Gropp, Y. Ma, C. Zhu, O. M. Yaghi, *J. Am. Chem. Soc.* **2020**, *142*, 20335.